



# **Study of the calorimeter detector response to particles relevant for Dark Photon studies at the FASER experiment**

---

Moisés Barberá Ramos

Master of Physics Thesis

University of Liverpool, Liverpool, UK

May, 2020





Faculty of Science and Engineering

Department of Physics

Thesis

**Study of the calorimeter detector response to  
particles relevant for Dark Photon studies at the  
FASER experiment**

by

**Moisés Barberá Ramos (201168940)**

---

A Thesis Submitted in partial fulfilment of the requirements for the degree of

**Master of Physics**

Under the supervision of Prof. Monica D'Onofrio and Dr. Carl Gwilliam

May, 2020

**Moisés Barberá Ramos**

*Study of the calorimeter detector response to particles  
relevant for Dark Photon studies at the FASER experiment*

Master of Physics - MPhys (Hons) -, May 2020

Supervisors: Prof. Monica D’Onofrio and Dr. Carl Gwilliam

**University of Liverpool**

*Faculty of Science and Engineering*

Department of Physics

Group of High Energy Physics

University of Liverpool

L69 3BX Liverpool

## Declaration of Authorship

I, MOISÉS BARBERÁ RAMOS, declare that I completed this thesis, "**Study of the calorimeter detector response to particles relevant for Dark Photon studies at the FASER experiment**", on my own and that the information which has been directly or indirectly taken from other sources has been noted as such. Neither this nor a similar work has been presented to an examination committee.

Liverpool, UK, May 14, 2020

MOISÉS BARBERÁ RAMOS (M.B.R.)

## Acknowledgments

First of all, I would like to thank my main supervisor Prof. Monica D’Onofrio for giving me the wonderful opportunity to complete my Master’s Thesis under her supervision. After welcoming me in this exciting project, I cannot thank her enough for our discussions, her advice, ideas and guidance through the totality of the project. Thank you for your enthusiasm for the study of particle physics and specially for introducing me to the research of Dark-Matter indicators at this new collaboration called FASER. Thank you for giving me the opportunity to grow on this field of research. Working with you has been a true pleasure and a motivation.

Also, I would like to thank my second supervisor Dr. Carl Gwilliam and my colleague Alasdair, who has also worked on FASER during his Master’s thesis. Thanks for your inputs and coding advice that helped me complete this project.

I extend my sincere gratitude to the department of Physics at the University of Liverpool for providing the resources to do my research as well as to the FASER collaboration for letting me contribute to this innovative and exciting research.

Further I would like to give special thanks to Prof. Carsten Welsh, Head of Department of Physics at the University of Liverpool, I met you when I first moved in to the UK during my first year at University; thank you so much for your help and support through these 4 years, it has meant a lot.

I would also like to give special thanks to Prof. Rolf Dieter Heuer, our casual meetings every several years, since 2013 when we met in Geneva, motivated me to pursue the degree of Physics and to contribute to the scientific community through every piece of work I have done. For seeing you again around the world.

Lastly, I would like to thank my family, your unconditional love, moral support and optimism have helped bring home a bit closer to me.

# Abstract

The FASER experiment has potential to detect popular models of light, long-lived particles which have been proposed in the context of Physics Beyond Colliders' studies, expanding the LHC discovery reach. The new physics models satisfy dimensions for interactions from the Standard Model (SM) and imply the presence of a dark sector weakly interacting with the SM. FASER will focus on looking for one of the most likely dark-partner of SM particles, the Dark Photon.

This master's thesis focuses on the early stages of FASER, where it's imperative to understand its functionality and its characteristics to parameterize the response of the experiment scintillator/lead calorimeter to incoming charged or neutral particles. This study is specially relevant for the experiment as for very high energies (between 100 GeV - 1 TeV [8]), we expect to record electromagnetic showers coming from photons and electrons as they go through the thick lead layers in between the scintillators composing the calorimeter.

Calorimeter detector simulations were developed using the Geant4 software, and the response of electrons, photons, and muons was studied in terms of deposited energy as a function of their initial energy, integration location, and beam direction. Two geometries have been studied, a simple one simulating the calorimeter as a single module and a more complex one with four modules and intermediate non-reactive regions in between. Detailed studies of the electrons (and positrons) energy response are presented, as well as comparisons with photons, muons and pions.

# Contents

	Page
Declaration of Authorship . . . . .	v
Acknowledgments . . . . .	vi
Abstract . . . . .	vii
List of Figures . . . . .	x
List of Tables . . . . .	xix
List of Abbreviation . . . . .	xxi
Introduction . . . . .	1
<b>1 The FASER experiment and the search for new physics</b>	<b>3</b>
1.1 The Standard Model of Particle Physics and Beyond . . . . .	4
1.2 Physics Motivation for FASER . . . . .	9
1.3 The FASER experiment within the LHC complex . . . . .	12
1.4 The FASER experiment . . . . .	16
<b>2 Calorimetry</b>	<b>19</b>
2.1 General detectors . . . . .	19
2.2 Electromagnetic calorimeter . . . . .	21
2.3 FASER's calorimeter . . . . .	24
<b>3 The Geant4 simulation</b>	<b>26</b>



3.1	Geant4 . . . . .	26
3.2	A simple calorimeter Layout . . . . .	31
3.3	A more realistic layout . . . . .	33
3.4	Material dependence and multiple scattering . . . . .	36
3.5	Simulated data . . . . .	39
<b>4</b>	<b>Simulated data analysis: electrons and photons</b>	<b>42</b>
4.1	Data analysis description . . . . .	43
4.2	Analysis for electrons . . . . .	47
4.2.1	Energy deposit . . . . .	47
4.2.2	Angular scan in simple layout . . . . .	51
4.2.3	Angular Scan in the more realistic layout . . . . .	53
<b>5</b>	<b>Simulated data analysis: muons and pions</b>	<b>61</b>
5.1	Muon studies . . . . .	61
5.1.1	Parameterizations of the Energy Loss on muons . . . . .	63
5.2	A word on pions . . . . .	68
<b>6</b>	<b>Summary and conclusion</b>	<b>71</b>

# List of Figures

1.1	Figure credited to Daniel Dominguez/CERN. As mentioned, the Standard Model shows leptons (electrons, electron neutrinos, mu, mu neutrinos, tau and tau neutrinos), quarks (up, down, top, bottom, beauty and charm), force-carrier particles (photon, gluon, W and Z bosons) and the Higgs Boson. . . . .	6
1.2	Feynman diagram for the LLP production process of a neutral meson, $\pi^0$ , decaying into a standard photon and a Dark Photon. . . .	10
1.3	Feynman diagram for the decay of the Dark Photon, $A'$ , decaying into a pair of $e^+ - e^-$ . [61] . . . . .	11
1.4	(a) Differential meson production rate in each hemisphere in the $\theta$ plane, where $\theta$ and $p$ are the meson's angle with respect to the beam axis and momentum, respectively. The bin thickness is 1 over 10 of a decade along each axis. We show the $\pi^0$ spectrum, obtained via EPOS-LHC [69]. (b) FASER's reach in the search for Dark Photons, the gray-shaded regions are excluded by current bounds, and the projected future sensitivities of other experiments are shown as colored contours. . . . .	11

1.5	Layout of the LHC, in red the CMS and ATLAS experiment have been highlighted [33]. At the interaction point 5, IP5, the CMS is located and at interaction point 1, IP1, we find ATLAS. . . . .	13
1.6	In the figure, [38], the red star highlights the future location of FASER, 480 meters away from ATLAS IP1, where the LHC tunnel starts to curve, inside the service tunnel TI12 as highlighted in yellow. . . . .	14
1.7	In the figure, [11], the upper panel shows how FASER is located right at the point where the LHC tunnel starts to curve, at a position 480m along the beam collision axis line of sight (dotted line). The left side panel, with an extreme difference in horizontal and vertical scales, represents particles produced at ATLAS IP1 and how charged particles are deflected by the LHC magnets while neutral hadrons are absorbed by either the TAS (Target Absorbers) or TAN (Target Absorber Neutral) [25], but LLPs pass through the whole infrastructure without interacting. Finally, the right side panel show LLPs occasionally traveling and decaying within FASER. . . . .	15
1.8	In purple is the scintillator veto, in red the 1.5m long decay volume, in green the 2m long spectrometer and finally, in blue is the EM calorimeter. . . . .	17

1.9	Design of FASER. The first section on the left is the mentioned Veto scintillator, the following red rod corresponds to the volume decay, the two final red rods are the spectrometer and the final blue section is the EM calorimeter. In addition, key components of the detector such 0.6 Tesla dipole magnets, triggering stations for the timing and preshower as well as silicon strip tracking stations have been identified. . . . .	18
2.1	Representation of the showers, in blue, generated by a charged particle, an electron in this case, entering an EM calorimeter. . . .	22
2.2	Schematic view of one 1 of the 4 LHCb's ECAL modules used at FASER's calorimeter. Provides up to 1% accuracy in energy $\sim 1$ TeV. . . . .	25
3.1	Code use in Geant4 to simulate an incoming particle based on the characteristics described in the .in file (here representing an electron at 100 GeV). . . . .	29
3.2	In green and entering the calorimeter from left to right (a) is an electron at 100 GeV accessing the calorimeter with coordinates (0, 0) and creating a shower, a view of the cross-section is also presented (b). . . . .	31
3.3	Sketch of the first three layers (from 0 to 2) for a single module calorimeter. Each layer shows how it is divided in absorbers and gaps which are then used to record the energy deposit of the particles. . . . .	32

3.4	Cross-section of a single module calorimeter, defined with the white line square, showing the deposited energy of a simulated electron of 1 TeV accessing the calorimeter with coordinates (0, 0). Showers shown in green. . . . .	32
3.5	The energy deposits of an electron of 100 GeV are shown in these two figures which share a negative-skewed like distribution. (a) shows the energy deposited in the absorber and (b) the energy on the gap. The X axis shows the energy in MeV and the Y axis the number of events. . . . .	33
3.6	Three different views of the realistic layout with an electron of 100 GeV accessing the calorimeter at entrance coordinates of (0, 0) and a shift on the angle of 50 mrad. The first figure (a) provides a better look at the centered entrance of the particle, represented in red. As the particle moves through the air gap between modules it does not generate showers. Figure (b) presents with annotations the angle shift and the size of the gap. A better look at the trajectory of the particle due to the shift angle is shown in the third figure (c). . . . .	35
3.7	Data of photons (light purple), anti-Pions (cyan), Pions with msc (yellow), Pions without msc (Green) and electrons with msc (solid pink) and without multi-scattering (red), all at 100 GeV, depositing energy on the absorbers (a, c) and gaps (b, d) of two different calorimeters. The first line (a, b) refers to a plastic calorimeter and the bottom line (c, d) refers to a calorimeter made out of liquid argon, both based on the single module configuration. A logarithmic scale has been used in the Y axis. . . . .	38

3.8	Two case scenarios expected when running simulations, created with entrance coordinates at origin (0, 0) at 100 GeV. The top layer shows the showers of electrons (a) and muons (b) interacting with the material of a single module calorimeter. On the bottom layer simulations are performed on the more realistic layout, particles moving across the air gap and not interacting with the material of the module deposit a small amount of energy and create small or non-existent showers. Electrons (c) and muons (d) (shown with a depth perspective). . . . .	40
4.1	Gaussian distribution for 3 different combinations of parameters. .	43
4.2	Crystal Ball distribution with 3 different combinations of the parameters. . . . .	45
4.3	Studies comparing the Energy Gap mean using a Gaussian and a Crystal Ball fit. . . . .	46
4.4	Studies on the sigma over E <sub>gap</sub> mean and the alpha parameters using the Crystal Ball function. . . . .	46
4.5	Simulation of a 100 GeV electron across the calorimeter, energy versus number of events. In the left (a), energy is deposited in the absorber, the energy released by particles undergoing msc is close to the one released by optimal particles without msc. On the right (b), is the energy deposited on the gap, differences between msc and no msc place the energy peaks almost 4000 MeV apart. . . . .	48

4.6	Using a crystal ball fit, this figure shows the fraction of energy deposited as a function of injected energy. The graphs present data from electrons with msc (Red) and without msc (Pink). An over-fit can be expected at 100 GeV with no msc electron data. . . .	49
4.7	Using a crystal ball fit, this figure shows the injected energy minus the sum of energy recorded by the gap and absorber, divided by the injected energy. The graph presents data from photons (Green) and electrons with multi-scattering (Red) and without multi-scattering (Pink). An expected overfit can be expected at 100 GeV with no multi-scattering. . . . .	51
4.8	Here [6], a pair electron-positron decaying from a Dark Photon is described showing an increasing angle aperture between the pair. We can expect for increasing entrance angles, that pairs have the risk of leaving the detector before reaching the calorimeter or the end of it. . . . .	52
4.9	Angular scan on ideal calorimeter using a crystal ball fit with entrance coordinates (0, 0). From 0 mrad to 100 mrad angle shift there is approx. 1.5% deviation in energy deposited. . . . .	53
4.10	Presents the coordinates studied in this thesis, numbered in order, for the three cases described in this section. Also orders alphabetically the 4 modules of the calorimeter. . . . .	54
4.11	Case scenarios for the -100 mrad (a, b) and 100 mrad (c, d) of the angular scan showing how the beams move closer to the edges of the modules. . . . .	56

4.12	Shows the fraction of energy deposited from 100 GeV electrons entering the calorimeter at coordinates (10 mm, -10 mm) and as a function of changing angle. Analysed using the Gaussian mean. .	57
4.13	Visualizations for 3 different angles in the range studied. (a) shows an entrance angle of -100 mrad, the beam moves across the gap between modules A and C. (b) is a close-up look at a particle with -50 mrad trajectory, compensates the shift angle moves through the centre of the calorimeter. (c) shows an entrance angle of 100 mrad, the beam moves across the gap between module B and D. .	58
4.14	Fraction of energy deposited from electrons entering the calorimeter at coordinates (0 mm, 0 mm). Important to notice these figures have been extremely zoomed in as there is a small fraction of deposited energy of the order of $10^{-6}$ . Both 100 GeV and 1 TeV data can be considered on the same range of impact. . . . .	58
4.15	Shows the fraction of energy deposited from 100 GeV electrons entering the calorimeter at coordinates (0 mm, -10 mm). (a) shows the total fraction of energy deposited and (b) that of the gap. Errors are too small to be seen. . . . .	59



4.16	3 different visualizations for 3 different angles in the range studied. In the left (a) we see the shower for a beam with entrance angle -100 mrad with a strong interaction in all modules. In the centre (b), we have a close-up look at a particle with -50 mrad trajectory, this one compensates the shift angle and places the beam right in the 1.2 mm air gap between module C and D. On the right (c) a view at a 100 mrad simulation with a shower interacting mostly in module B and D, but a part of the energy is lost outside the calorimeter or in the gap. . . . .	60
5.1	Fraction of events in tails for muons with 20 GeV (a) and 1 TeV (b). We observe a higher percentage of events recorded above small thresholds in high energy muons, 2.8% for (a) versus a 31% for (b). Also, for 20 GeV muons there are barely any recorded events above the 50 GeV threshold while for 1 TeV muons we still record events in tails above 500 GeV. . . . .	63
5.2	5 simulated muons with energies increasing from 20 GeV to 1 TeV, the fraction of events in tails above the selected thresholds increase exponentially. . . . .	64
5.3	Shows the landau distribution for some relative probability. It differentiates the most probable energy loss (characteristic of this function) and the mean energy loss (given by the Gaussian fit). . .	65

5.4	Visualization of the Landau distribution as applied on the absorber and gap energy deposits for a 20 GeV muon (a) and for a 1 TeV muon (b). It is observable how for low energies the Landau distribution presents a perfect fit but becomes more inaccurate for high energies. . . . .	66
5.5	Parametrization of the MPV energy loss, $E_{loss}^{mpv}$ , done applying equation 4.3 (a) and the width parameter of energy loss, $\sigma_{loss}^{mpv}$ , done applying equation 4.5 (b); where the Landau distribution was considered as a function of energy. In red is the fit on the gap and in green the fit on the absorber. These consider muons of different energies accessing a single module layout calorimeter. . . . .	67
5.6	Fraction of energy deposited in the gap by the electron, photon and neutral pion using their Gaussian mean. . . . .	69
5.7	Results from simulating a pion (a) and an anti-pion (b) at 100 GeV moving across the FASER Detector, in the X axis we find the energies and in the Y axis the number of events. Both figures show a similar behaviour where the energy deposited in the detector is around 220-250 MeV. The low and long tails extend close to 80 GeV, outside the ranges in this visualization. . . . .	70

# List of Tables

3.1	An approximate comparison on how long it takes to generate files for electrons and muons based on their incoming energy and on how much they interact with the material of the module. Files for photons would share the same timing as electrons. . . . .	41
5.1	Shows the parametrization values for the MPV Energy loss absorber and gap data fit obtained for the equation presented above which can be seen to fit the landau distribution on the upper side of figure 5.5a. . . . .	67
5.2	Shows the parametrization values for the width loss absorber and gap data fit obtained for the equation presented above which can be seen to fit the landau distribution on the upper side of figure 5.5b.	68

6.1	This table, extracted from FASER’s research on the physics reach of the detector for Long-Lived Particles [10], shows a variety of benchmark models aimed to be studied by the FASER collaboration during FASER or FASER 2. The table presents the labels of each benchmark as well as their PBC labels and references were they have been previously studied. The discovery potential of FASER and FASER 2 covers candidates with renormalizable couplings like dark photons, dark Higgs bosons or HNLs (Heavy Neutral Leptons); also potential to discover ALPs (axion-like particles) with their corresponding couplings; dark pseudoscalars with Yukawa-like couplings; and others. . . . .	83
-----	---	----

## List of Abbreviations

**LHC** Large Hadron Collider

**SPS** Super Proton Synchrotron

**LEP** Large Electron-Positron

**LLP** Long-Lived Particle

**HNL** Heavy Neutral Leptons

**p-p** proton-proton

**LOS** Line Of Sight

**TAS** Target AbsorberS

**TAN** Target Absorber Neutral

**IP** Interaction Point

**BF** Background Field

**MIP** Minimum Ionising Particles

**msc** multi-scattering

**PBC** Physics Beyond Collider

**WIMP** Weakly Interacting Massive Particle

# Introduction

Proposed in August 2017 [47] and approved by CERN in March 2019 [34], FASER, the ForwArd Search ExpeRiment, is a new type of detector placed at the LHC. With cylindrical volume, a transverse radius of 10 cm covering the mrad regime ( $\eta > 9.1$ ) and a length of 1.5 metres [47], this inexpensive detector is expected to study new hypothetical particles which decay far from the primary interaction point. Among these particles, referred to as long-lived particles (LLP), could be the Dark Photons as part of a new dark sector weakly interacting with the Standard Model sector. Dark photons are expected to be produced in proton-proton (p-p) collisions at ATLAS [57] interaction point and their decay products could be collected by FASER.

While FASER focuses on the search for Dark Photons starting in 2021 during RUN 3, FASER 2 (expected to be introduced in RUN 4 and with a radius of 1 meter) will also focus on Dark Higgs Bosons and heavy neutral leptons (HNLs), all of which are Dark matter indicators [56].

Dark Photons are hypothetical particles proposed as a force carrier similar to the photon of electromagnetism but potentially connected to dark matter [1].

Dark photons can decay in pairs of electrons/positrons, muons or hadrons. It is important to understand how these particles can be identified and characterised. While charged particles in general are reconstructed in the so-called tracking system, electrons and photons' energies are measured using the calorimeter. In this thesis, we focus on the simulation of the FASER calorimeter, and we study the way electrons and photons energies can be measured. Studies on muons and pions are also presented. Energy response depending on incident position and angle are studied. This study gives information on the required specifications of the

FASER calorimeter.

Chapter 1 presents an introduction on the Standard Model and physics beyond this model where FASER's research focus is and also, an introduction to the FASER experiment in general. Chapter 2 is a summary on calorimetry and what detection technologies FASER uses. Chapter 3 introduces the Geant4 software used to simulate the response of the detector to incoming particles and what different types of design layouts have been explored in this thesis. Chapter 4 shows the wide variety of tests performed, the methodologies and results obtained. It includes the study of electrons (and photons)' response with the detector and angular dependencies of the deposits. Chapter 5 shows results considering muons and pions. Finally, Chapter 6 summarises the work done in this research and the impact of our findings on the FASER experiment.

# Chapter 1

## The FASER experiment and the search for new physics

While the interest in researching undiscovered particles arises, new experiments are being proposed to expand the scientific reach of CERN's accelerator complex. As part of the Physics Beyond Collider (PBC) study [16], FASER helps diversify LHC's focus and will address unanswered questions with a new approach [56].

FASER will complement existing searches for dark matter at the LHC from 2021 to 2023 initially. Looking for light, long-lived and weakly interacting particles (they possess a longer lifetime) coming from experiments already present at the LHC, FASER extends the discovery potential of CERN to several new particles.

Although the LHC experiments are capable of looking for invisible final states by looking for mediator or dark matter production in association with one or more visible objects, their sensitivities are limited to SM-mediator couplings  $\epsilon$  of the order of  $10^{-1}$  [14].



The existence of dark matter is inferred by cosmological studies through gravitational interactions. Many hypothesis are made on its nature. A traditional definition would consist of a heavy particle interacting through the weak force, referred to as Weakly Interacting Massive Particles (WIMPs), predicted by R-parity-conserving supersymmetry [65]. This motivates the search for dark matter scattering in underground detectors, for dark matter annihilating in the cosmos and for its production in high-energy colliders [45]. FASER, as a detector itself, of course, focuses on the latter motivation.

In this chapter, we introduce the current status of the Standard Model, how it stands on the search for dark matter and the role FASER plays in finding answers to current unknowns as well as an introduction to what this experiment does and where it will be based within CERN to create the biggest impact.

## **1.1 The Standard Model of Particle Physics and Beyond**

Since 1930s, with the discoveries of particles providing a closer look at their own structure [71, 23, 9, 64], physicists have been making remarkable contributions into the fundamental structure of matter; including the realisation that everything in the universe is made from a few building blocks, the fundamental particles, which later would be found out to be governed by four fundamental forces [59].

Since then, and after the start of the development of the Standard Model in the 1970s, this model encapsulates the best understanding of the scientific community about these fundamental particles and three of the four fundamental forces, gravity is not yet fully explained by this model. So far, it has successfully ex-

plained almost all experimental results and precisely predicted a wide variety of phenomena.

This Standard Model of particles features the following characteristics [73]:

- It works to include quantum mechanics and relativity so it is therefore based on quantum field theory, QFT (as it tries to incorporate the predictions about gravity as a fundamental force).
- Predictive power based on regularisation of divergent quantum fields and the re-normalisation of couplings.
- All fundamental forces, electromagnetic, weak, strong and gravitational; are related to symmetries and are described by Abelian and non-Abelian gauge theories.
- The particles described in the model are divided in three families or generations.
- Masses of particles are generated either by confinement or spontaneous symmetry breaking.

The Standard Model mathematically lays out the 17 building blocks of nature including: six quarks, six leptons, four force-carrier particles and the Higgs Boson, all ruled by the electromagnetic, weak and strong force. A schematic view provided by CERN is presented in figure 1.1:

Particles with electric charge are influenced by electromagnetic interactions (described by quantum electrodynamics, QED) and their force carrier particle is the photon,  $\gamma$ ; particles with a weak charge are influenced by weak interactions and their force carrier particle are the W and Z bosons,  $W^+$ ,  $W^-$  and  $Z^0$ . The

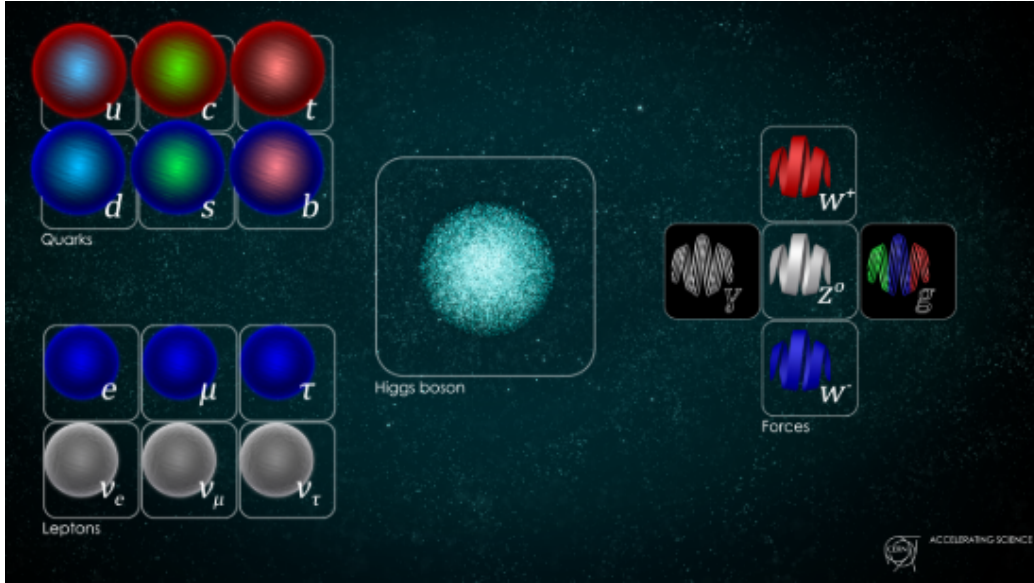


Figure 1.1: Figure credited to Daniel Dominguez/CERN. As mentioned, the Standard Model shows leptons (electrons, electron neutrinos, mu, mu neutrinos, tau and tau neutrinos), quarks (up, down, top, bottom, beauty and charm), force-carrier particles (photon, gluon, W and Z bosons) and the Higgs Boson.

colour charge is influenced by the strong interaction (described by quantum chromodynamics, QCD) and their force carrier particle is the gluon,  $g$ . Finally, the Brout-Englert-Higgs (BEH) field acts, inducing spontaneous symmetry-breaking and hence gives mass to all particles with which it interacts [48].

The mathematical representation of the model starts from the use of the free particle Lagrangian and replaces the ordinary derivative by the covariant derivative containing two sections, the kinetic energies of the gauge fields and the fermion kinetic energies. Following this and the theoretical basics which identify the key elements of the equation, renormalizable quantum field theory + gauge symmetries + spontaneous symmetry breaking and the Higgs mechanism [67] we can get a simplified version of the Lagrangian explaining the whole model in a couple of

lines:

$$\begin{aligned}
\mathcal{L} = & -\frac{1}{4}F_{\mu\nu}F^{\mu\nu} \\
& + i\bar{\psi}\not{D}\psi \\
& + \bar{\psi}_i y_{ij} \psi_j \phi + h.c. \\
& + |D_\mu \phi|^2 - V(\phi)
\end{aligned}$$

Where the first line refers to the Gauge fields defined by field strength tensors [18] forming the kinetic term of the equation and its Gauge field tensors, which contribute further to the rest of components of the equation, are described in table 1.1.

Symmetry	Gauge Boson
U(1)	Neutral gauge boson
SU(2)	3 Heavy vector bosons
SU(3)	8 Gluons

The second line,  $i\bar{\psi}\not{D}\psi$ , refers to the kinetic term for a Dirac fermion where  $\psi$  refers to any, or all, Dirac fermions in the SM.

The third line refers to the quark dynamical term where (h.c.) means Hermitian conjugate of proceeding terms  $\bar{\psi} = (\text{h.c.}) \psi$ .

The fourth and final line of the equation refers to the Higgs dynamical and mass term, where  $\phi$  is a 2-component complex Higgs field [29].

Despite its great predictive power, however, the Standard Model leaves open questions [43]:

- **Why do neutrinos have mass?**
- **What is dark matter?** While the Standard Model is an effective method to describe the matter around us, it composes roughly 5% of the entire universe. On the other hand, Dark Matter is thought to make up 27% of the universe and it's not described in the SM.
- **Why is there so much matter in the universe?** And what does this matter-antimatter asymmetry mean?
- **Why is the expansion of the universe accelerating?** The answer here is thought to be related with the unexplained property of space-time called dark energy which is thought to make up around 68% of the universe.

As these questions, and many more, are not described by the Standard Model, the research around them lays under the concept of Physics Beyond the SM.

FASER aims to detect dark matter indicators but as we said dark matter is still unknown, although there is evidence for its existence, in the form of non-baryonic contributions to the abundance of matter in the universe [21], indicators have not yet been identified that explain what it is.

So far, only gravitational interactions have been studying towards solving this unknown but this process can only provide information about the abundance of dark matter not about the form of it.

One of the most important new particles arising from hypothetical dark sectors is the Dark Photon,  $A'$ . Here a new U(1) dark force closely related to the electromagnetic (EM) force can be introduced into the SM, where  $A'$  would be the force mediator coupling to dark matter (or matter) and carrying dark charge.  $A'$  could kinetically mix with the photon so it could be observed in the spectra of

final states produced by the EM current. This mixing is potentially involving high mass particles connecting the visible and dark sectors [22].

## 1.2 Physics Motivation for FASER

FASER expects to identify Dark Photons,  $A'$ , which may act as a mediator for Dark Matter. The theory behind this signal is described by 2 parameters mainly; being the mass of the Dark Photon ( $m_A$ ) and its coupling ( $\epsilon$ ).

Dark photons can be long-lived: they could be produced at the ATLAS interaction point (IP) and then decay after traveling for a while in the very forward region, usually, with very high energies (TeV).

Dark Photons could decay into an  $e^+ e^-$  pair (with a probability of 45%), a  $\mu^+ \mu^-$  pair (45%) or a  $\pi^+ \pi^-$  pair (smaller probability of 10%) within FASER and be identified as one or two very high energy electromagnetic clusters. Decay products of Dark photons (particularly electrons) can be identified within the electromagnetic calorimeter.

As particles collide in ATLAS, at point IP1, it is expected that the leading production mechanism will typically be the decays of the lightest mesons that are kinetically allowed to decay to LLPs.

During LHC Run 3, with an expected integrated luminosity of  $150 \text{ fb}^{-1}$ , we expect about  $2.3 \times 10^{17}$  neutral pions, which may then decay (very rarely) into a combination leading to a Dark Photon,  $A'$ , see figure 1.2. Typical signals usually follow the background field (BF) close to  $\epsilon^2$  or close to  $10^{-10}$  [7].

From the production of  $\pi^0$  in the LHC collisions the acceptance of this particle in FASER is around 2%.  $\pi^0$  produced in FASER are very energetic, generally E

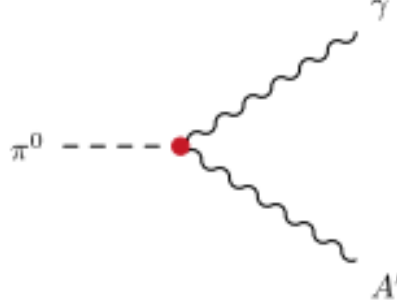


Figure 1.2: Feynman diagram for the LLP production process of a neutral meson,  $\pi^0$ , decaying into a standard photon and a Dark Photon.

$> 1$  TeV, figure 1.4a and while FASER acceptance covers just  $(2 \cdot 10^{-6})$  % of the solid angle, we should expect around  $O(10^{15})$  of these mesons produced in FASER acceptance during Run 3 [20].

After the production of the Dark Photon, in the relevant region of signal parameter space it is a long lived particle which travels approximately  $O(100\text{m})$  before decaying thanks to the huge boost received from the  $\pi^0$ .

The  $A'$  then decays into fermion/anti-fermion pairs kinematically available:  $\mu^+ - \mu^-$ ,  $\pi^+ - \pi^-$  but mostly  $e^+ - e^-$  pairs, figure 1.3, which is present for most of the  $m_{A'}$  range relevant for FASER. Despite the small size of FASER, 1.5 meters long and placed 480 meters away from the point of collision, we should expect a significant number of signal events from  $A'$  decays, figure 1.4b.

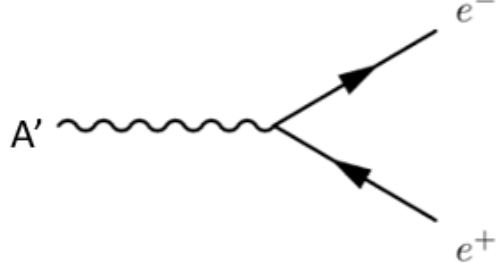
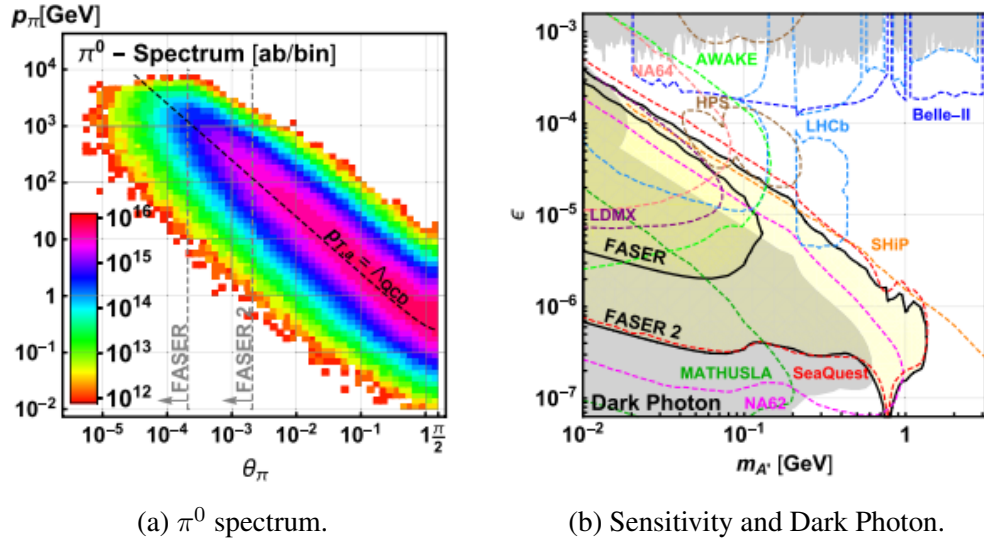


Figure 1.3: Feynman diagram for the decay of the Dark Photon,  $A'$ , decaying into



(a)  $\pi^0$  spectrum.

(b) Sensitivity and Dark Photon.

Figure 1.4: (a) Differential meson production rate in each hemisphere in the  $\partial \theta$ ;  $p_T$  plane, where  $\theta$  and  $p$  are the meson's angle with respect to the beam axis and momentum, respectively. The bin thickness is 1 over 10 of a decade along each axis. We show the  $\pi^0$  spectrum, obtained via EPOS-LHC [69]. (b) FASER's reach in the search for Dark Photons, the gray-shaded regions are excluded by current bounds, and the projected future sensitivities of other experiments are shown as colored contours.



### 1.3 The FASER experiment within the LHC complex

CERN is the world’s largest particle physics laboratory and its core is the LHC, a 27 km long ring of superconducting magnets with a number of accelerating structures boosting the energy of particles along the way. This is one of largest scientific instruments ever built and the LHC physics program is considered as one of the most successful experimental programs in science, a statement supported by discoveries such the Higgs boson in 2012 by two [4, 24] of the four main experiments located along this circular accelerator, the CMS and ATLAS experiments highlighted in figure 1.5.

FASER is being installed during Long shutdown 2 and will be ready to operate during Run 3 starting in 2021. This experiment is joining the LHC at a time where the High Luminosity LHC upgrade is taking place, aiming at constraining, and possibly discovering, a wide variety of new physics (NP) scenarios with imprints at the TeV scale. This upgrade in the LHC expects to collect an integrated luminosity of up to  $3 \text{ ab}^{-1}$  of data [3] from p-p collisions at a centre-of-mass (c.o.m.) energy of 14 TeV with the goal of accessing new phenomena.

Protons will collide at the center of ATLAS and CMS where the resulting decays, electrons and photons, are reconstructed from energy deposits in the electromagnetic calorimeter and information from the inner tracker; and muons are reconstructed combining muon spectrometer and inner tracker information. In the meantime, LLPs would fly away from its production vertex, meaning that if we take the mixing term,  $\epsilon^2$ , as the ratio of the dark force strength to the EM force strength, for small values of  $\epsilon^2$ , theoretical Dark Photons could not be detected in

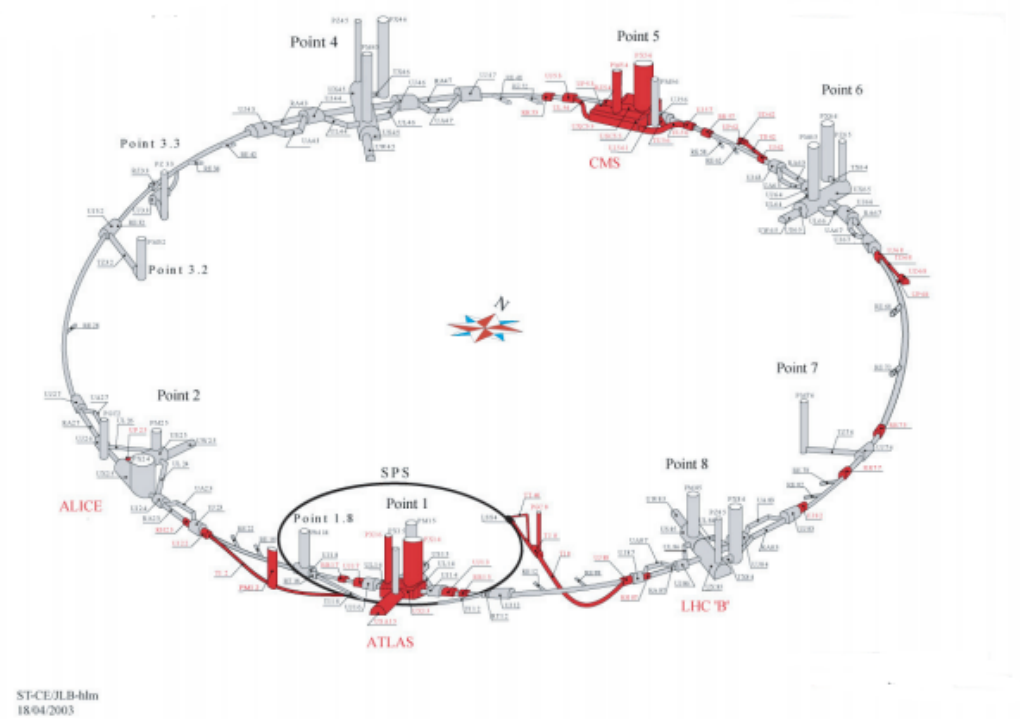


Figure 1.5: Layout of the LHC, in red the CMS and ATLAS experiment have been highlighted [33]. At the interaction point 5, IP5, the CMS is located and at interaction point 1, IP1, we find ATLAS.

the current experiments but instead further away from its production vertex [72].

To fulfill this goal of detecting Dark Photons, FASER will take the challenge of aiming to detect the decays of possible Dark Photons coming from ATLAS.

FASER will be placed approximately 480 meters away from ATLAS interaction point 1, along the beam collision axis line of sight (LOS), in the side tunnel TI12, see figure 1.6, an empty tunnel previously used to connect the Super Proton Synchrotron (SPS) to the Large Electron-Positron (LEP) accelerator [47].

The beam collision axis passes across TI12 near to where it starts to curve

and merges with the main LHC tunnel. The LOS, previously mentioned, enters TI12 just below the tunnel floor meaning that, in order to align it with the FASER detector, a trench of approximately 45 cm must be excavated [11].



Figure 1.6: In the figure, [38], the red star highlights the future location of FASER, 480 meters away from ATLAS IP1, where the LHC tunnel starts to curve, inside the service tunnel TI12 as highlighted in yellow.

As this detector expects to interact with light LLPs generated from ATLAS IP1, there are a series of components placed on its trajectory. A neutral particle absorber TAN is placed at a distance of 140m from ATLAS IP so that, if standard model particles produced from the same collision are not deflected by LHC magnets, then TAN (for photons, neutrons) will absorb them, see figure 1.7. Also, because of the FASER position, there is additional shielding consisting of 10 m of concrete and 90 m rock which LLPs must go through from ATLAS until they decay in FASER [55].

While this thesis explores particles decaying from a proposed Dark Photon, Dark Photons are only one of the mediators FASER, and its future successor

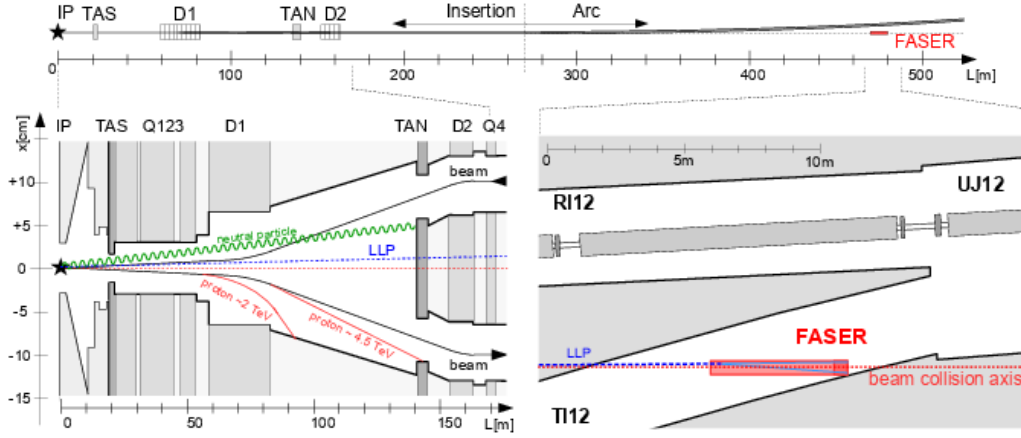


Figure 1.7: In the figure, [11], the upper panel shows how FASER is located right at the point where the LHC tunnel starts to curve, at a position 480m along the beam collision axis line of sight (dotted line). The left side panel, with an extreme difference in horizontal and vertical scales, represents particles produced at ATLAS IP1 and how charged particles are deflected by the LHC magnets while neutral hadrons are absorbed by either the TAS (Target Absorbers) or TAN (Target Absorber Neutral) [25], but LLPs pass through the whole infrastructure without interacting. Finally, the right side panel show LLPs occasionally traveling and decaying within FASER.

FASER 2, are expected to investigate as part of CERN's PBC study group [16]. Different benchmark models from this program have identified potential discoveries for the FASER experiment (FASER and FASER 2) including Dark Higgs Bosons, Heavy Neutral Leptons or Dark pseudo-scalars among others, see Appendix table 6.1.

Key differences in construction between FASER and FASER 2 include:

$$\begin{aligned} \text{FASER: } L &= 1.5 \text{ m, } R = 10 \text{ cm, } \mathcal{L} = 150 \text{ fb}^{-1} \\ \text{FASER 2: } L &= 5 \text{ m, } R = 1 \text{ m, } \mathcal{L} = 3 \text{ ab}^{-1} \end{aligned}$$

Where  $L$  refers to longitudinal length,  $R$  to radius and  $\mathcal{L}$  to luminosity.

## 1.4 The FASER experiment

New physics searches at the LHC focus on high transversal momentum,  $p_T$ , which is appropriate for heavy and strong interacting particles. These searches target particles with TeV-scale masses and  $O(1)$  couplings to the standard model (SM), but FASER, on the other hand, is interested in new particles that are much lighter and more weakly coupled [14].

Should these LLPs exist, detectors such ATLAS or CMS could not detect them since they would escape and travel hundreds of meters without interacting before decaying to visible particles, such as electrons and positrons. Because these particles are highly collimated, light and weakly-interacting particles leaving ATLAS will travel and decay in the process until these visible decays are detected by FASER 480 meters away from IP1, at a point where particles would have only spread around 10 cm in the transverse plane, making this small ( $\sim 0.05 \text{ m}^3$ ) and inexpensive ( $\sim 2\text{M}\$$ ) detector a great addition to the search for New Physics [38, 70].

Considering the tight deadline for this experiment, since it was approved in march 2019 [34] and must be installed to collect data for RUN 3 by 2021 [5], the FASER experiment runs under a restrictive philosophy. Despite these restrictions, including the limited budget and timeline which pushed to re-use components from other detectors like the LHCb's ECAL modules for the calorimeter, FASER also avoids some challenges usually present in bigger experiments, the trigger rate is now  $\sim 500\text{Hz}$ , there is lower radiation impact (due to dispersion function of LHC in TI12) and there is a low occupancy/event size [20].

In particular, FASER is using 4 ECAL modules spared from the LHCb collaboration to measure the electromagnetic energy in each event (up to 1% accuracy).

Also, the CERN scintillator lab is producing FASER's scintillators, used for vetoing charged particles entering the decay volume for triggering and as pre-shower. Vetoing in this experiment is expected to achieve a charged particle veto with an efficiency above 99.99%. Also, the trigger used here times the signal with respect to timing of the p-p interactions and uses the thin radiator in front to generate a photon showering and disentangle neutrino interaction in the ECAL modules [70].

In the FASER detector itself, as schematized in figure 1.8, consists of 4 key differentiated sections. The scintillator veto (placed to veto incoming charged particles including protons), the long decay volume section where the mother particle is expected to decay into the pairs that will be detected by FASER, the spectrometer and the electromagnetic (EM) calorimeter where particles deposit most of their energy in the form of showers.

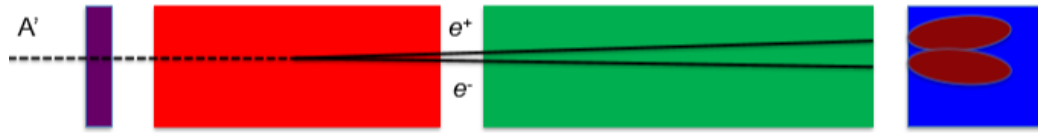


Figure 1.8: In purple is the scintillator veto, in red the 1.5m long decay volume, in green the 2m long spectrometer and finally, in blue is the EM calorimeter.

A closer look at FASER's components is shown in figure 1.9:

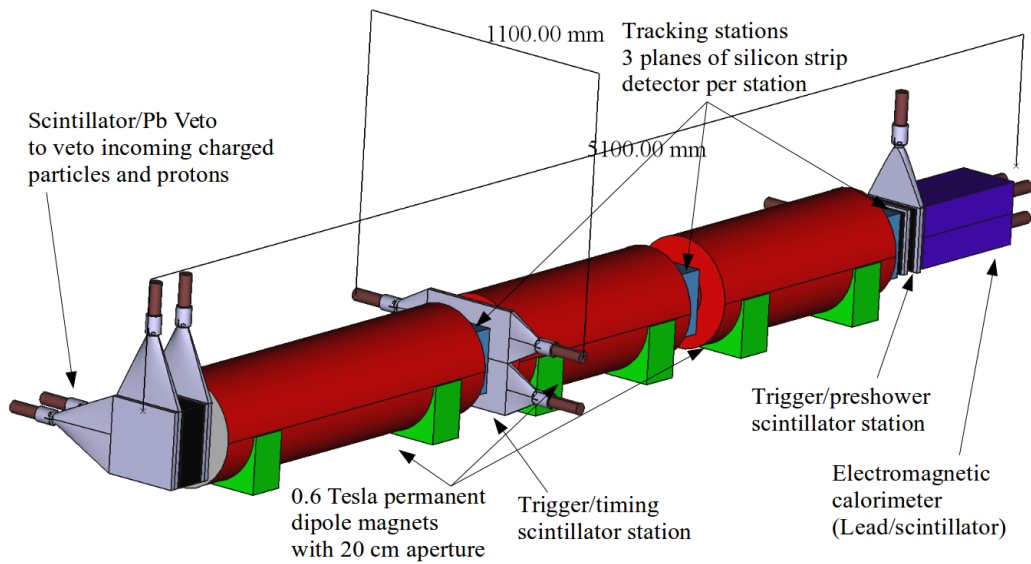


Figure 1.9: Design of FASER. The first section on the left is the mentioned Veto scintillator, the following red rod corresponds to the volume decay, the two final red rods are the spectrometer and the final blue section is the EM calorimeter. In addition, key components of the detector such 0.6 Tesla dipole magnets, triggering stations for the timing and preshower as well as silicon strip tracking stations have been identified.

# Chapter 2

## Calorimetry

In this chapter, the principles of particle detectors and in particular calorimeters are described.

Modern detectors at CERN like ATLAS and LHCb, which encompass a variety of tracking chambers and calorimeters surrounding completely the interaction point. In the case of FASER, the detector covers only one specific part of the space but it still includes a tracking system and an electromagnetic calorimeter. The principles of particle detectors and in particular of calorimeters are described in this Chapter.

### 2.1 General detectors

Detectors gather information about the particles that interact with them - including speed, mass, charge, trajectory - so that physicists can then reconstruct the particle's identity [30]. Nowadays, detectors consist of layers of subdetectors each designed with a particular focus looking for defined properties, as seen in the



previous figure 1.8 and described in more detail in the next figure 1.9.

Typical detectors used in particle physics include [42]:

- **Gaseous Ionisation Detectors:** here the walls of a chamber filled with gas is connected to the negative of an applied voltage and the center of the chamber through the anode. This configuration creates an electric field so, when charged particles pass across the chamber, they ionise the gas molecules creating anions and cations and hence generating a pulse that can be registered.
- **Semiconductor Detectors:** the most widely used detectors based on semiconductor materials are silicon detectors. They are the most common choice for tracking detector since they allow better resolution in reconstructing the path of charged particles with respect to gaseous ionisation chambers. The FASER tracking system is made of three layers of silicon detector modules.  
“
- **Calorimeters.** Calorimeters are made of various layers of material. Particles showers within the calorimeter and loose their energy, so that the energy deposited is measured. Calorimeters can be distinguished in electromagnetic (EM) calorimeters, targeting electrons and photons, and hadronic (HAD) calorimeters, used for hadrons and neutral particles. FASER will only have a EM calorimeter, which is the focus of this study and will be described in more details in the next sections.

## 2.2 Electromagnetic calorimeter

Calorimeters measure the properties of particles through absorption in a block of matter, this process is destructive, a common feature in this type of detector so, unlike other detectors like gaseous ionisation chambers, described above, the particles are no longer available for inspection once they interact with the calorimeter. Of course, this does not apply to muons or neutrinos which can penetrate a substantial amount of matter.

Calorimeters focus on measuring charged and neutral particles, their performance improves with energy and is constant over the full volume [53].

As mentioned in the previous section, there are two kind of calorimeters. On the one hand, electrons, photons and neutral pions,  $\pi^0$ , (which decay into photons) interact with the electrically charged particles of matter, and generate electromagnetic showers, so an electromagnetic calorimeter would be used to study these particles. On the other hand, hadronic calorimeters sample energy of hadrons (particles containing quarks) as they interact with the atomic nuclei instead [58, 53]

As explained, decays from Dark Photons are expected to be  $\mu^+ \mu^-$ ,  $\pi^+ \pi^-$  but mostly  $e^+ e^-$  pairs, so an EM calorimeter is going to be installed at FASER allowing it to reconstruct electrons, photons and neutral pions,  $\pi^0$ , by measuring the energy these deposit in the material of the calorimeter.

When charged particles like electrons or neutral particles like photons interact with this calorimeter, the EM showers are relatively compact and have a short shower depth so they are readily contained in a short distance, which is ideal for the small size of FASER. The size and shape of this shower is governed by the radiation length,  $X_0$ .

The radiation length is known to be the mean length (in cm) to reduce the

energy of an electron interacting with the EM calorimeter by the factor  $1/e$  [52] and depends on the material of the calorimeter, the density and the energy loss of incoming interacting particles.

Incoming particles deposit energy in the EM calorimeter and produce heat and showers of particles in the process 2.1. This energy is then converted into a response from the detector in the form of electric, thermal, optical and acoustic impulses. The response is then proportional to the energy deposited.

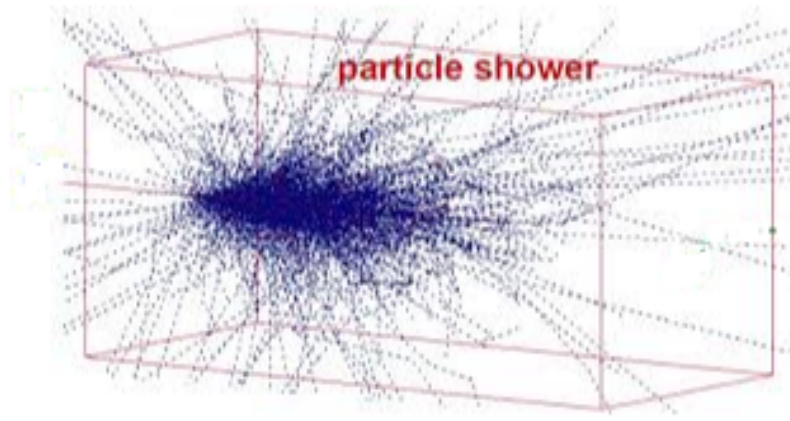


Figure 2.1: Representation of the showers, in blue, generated by a charged particle, an electron in this case, entering an EM calorimeter.

In EM calorimeters, we can identify how charged particles lose energy, as they move through matter, due to electromagnetic processes including: ionization (order of  $\alpha^2$ ) given by Bethe-Bloch formula [68], Bremsstrahlung (order of  $\alpha^3$ ) first calculated by Bethe and Heitler [17], and direct pair production (order of  $\alpha^4$ ) as described from QED calculations by Kelner and Kotov [49]; where  $\alpha$  refers to the fine structure constant  $1/137.036$ .

The precision with which the unknown energy deposited in the showers can be measured depends on the resolution of the detector and the fluctuations between

measurements, produced from variations in the signal of different events.

Here, the statistical errors from the variations in the track/length of the charged particles can be described as:

$$\left(\frac{\sigma}{E}\right)_{\text{statistical}}^{\text{electromagnetic}} \approx \frac{0.5\%}{\sqrt{E}} \quad (2.1)$$

Where  $E$  refers to the deposited energy and  $\left(\frac{\sigma}{E}\right)_{\text{statistical}}^{\text{electromagnetic}}$  refers to the statistical energy dependence in an electromagnetic calorimeter.

Also, EM calorimeters may experience sampling fluctuations described by:

$$\left(\frac{\sigma}{E}\right)_{\text{sampling}}^{\text{electromagnetic}} \approx 4\% \sqrt{\frac{1000\Delta E}{E}} \quad (2.2)$$

Where  $E$  refers to the deposited energy and  $\left(\frac{\sigma}{E}\right)_{\text{sampling}}^{\text{electromagnetic}}$  refers to the sampling energy dependence in an electromagnetic calorimeter.

Finally, the total energy resolution is based below  $\frac{\sigma}{\sqrt{E}} = 1\%$ , which is easy to achieve when we count with homogeneous EM calorimeters, but are more difficult to achieve in sampling ones [42].

These two types of electromagnetic calorimeter can be described as:

- **Sampling calorimeter:** in this case the material that produces the particle shower is different from the material that measures the deposited energy, typically alternating these two materials. A key advantage is that each material can be well suited for a given task; e.g. dense materials can be used to generate showers despite they are not suited to measure the energy deposits. A disadvantage is that as particles move across the material that does not measure the deposits, these are still losing energy, so the total shower must be estimated [27].

This is the case for FASER.

- **Homogeneous calorimeter:** the construction only considers materials that measure signals so the entire volume is sensitive.

## 2.3 FASER's calorimeter

The FASER calorimeter is made of 4 ECAL modules from the LHCb collaboration and which are separated by a gap which is expected to be 0.2 mm between top and bottom modules and  $\sim 1.2$  mm between left and right modules.

Each module features 66 layers of absorber/scintillator assigning 2 mm for the absorber made out of lead and twice as much, 4 mm, for the plastic scintillator. Plastic scintillators, when struck by an incoming particle, absorb the particle's energy and scintillate, for example re-emitting the absorbed energy in the form of light. These generate a high light output and a relatively quick signal, with a decay time of 2–4 nanoseconds [19]. Also, if the energy density of the particles is large, plastic scintillators may show light output saturation based on Birk's law [63].

Since FASER uses a sampling calorimeter, the described absorbers take some energy from the particles but do not measure the amount deposited. On the other hand, the gap/scintillator components are the ones measuring the energy deposited and hence the key focus on the studies presented in future chapters of this thesis where we will refer to the energy deposited in the scintillator as  $E_{gap}$  and the simulated energy in the absorber as  $E_{abs}$ .

With these 4 ECAL modules we accumulate 25 radiation lengths in the calorimeter. In terms of showers only transversal showers will be recorded, the calorimeter

does not provide information about longitudinal showers. Also, some resolution is lost because of the sampling configuration and the amount of energy lost by showers leaving the detector [37, 42].

A view of the ECAL module provided by LHCb can be seen in the following figure 2.2:

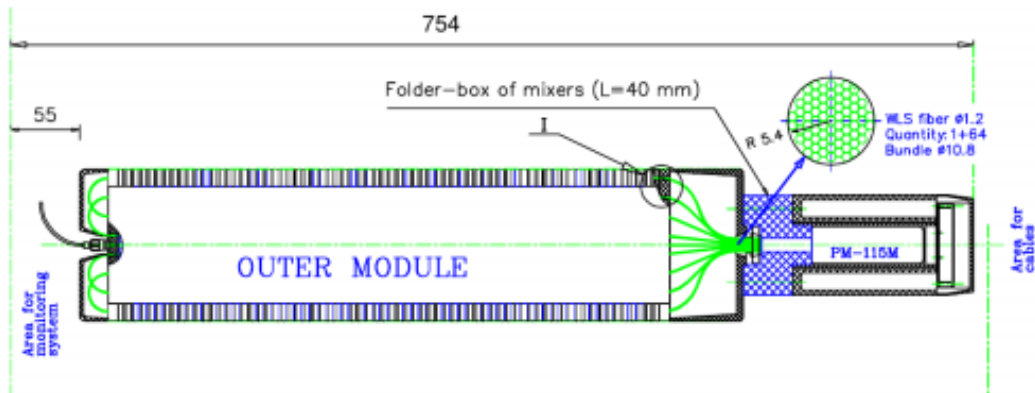


Figure 2.2: Schematic view of one 1 of the 4 LHCb's ECAL modules used at FASER's calorimeter. Provides up to 1% accuracy in energy  $\sim 1$  TeV.

# Chapter 3

## The Geant4 simulation

FASER is still been constructed and before being able to test it during RUN 3 in the LHC, we must generate a series of simulations to study FASER's calorimeter response to incoming particles. In particular, we are interested in studying the responses when different geometries and materials are used, for particles of different nature, energy and incident angle.

To satisfy this task we use the Geant4 software [12], which allows us to simulate particles entering a detector/calorimeter. Using this program, two geometry models have been utilised to understand the particle responses in different stages. In this Chapter, the Geant4 software and the layouts developed for the calorimeter are presented.

### 3.1 Geant4

This software program is a body of C++ code that models and simulates the interaction of particles through matter. The sectors where this program is applied

include high energy, nuclear and accelerator physics as well as some studies in the medical and space science field [32].

The Geant4 software package comes as a fundamental toolkit for High Energy Physics (HEP), it provides a wide coverage of the physics (including processes for shower parametrization, slow neutron, string models...) and automatically optimizes the user's geometrical description.

The package incorporates also event and track class objects and usability. Output files to be analysed to understand particles response are also made available under ROOT file format (see later).

Geant4 considers the following basic concepts [12]:

- **Run.** As an analogy of the real experiment, a run in the software simulates a run in the experiment and it starts with a "Beam On". This run is a collection of events which share the same detector conditions and, once activated, the detector geometry cannot be changed.
- **Event.** The event starts being processed so that the primary particles contained are pushed into a stack which once empty, stops processing the event.
- **Track.** A track is a snapshot of a particle and it is deleted if it goes out of the world volume (coded space for the simulation), if it decays, if it goes down to zero kinetic energy and no "at rest" additional process is required or if the user kills it. This concept is represented by three layers of class objects called: B4Track [Position, Volume, Track length, ...], B4DynamicParticle [Momentum, Energy, Local time, polarization, ...], B4ParticleDefinition [Mass, Lifetime, Charge, Decay Table, ...].



- **Step.** It has two points and also information on the change in quantities between the two step point of a particle (energy loss on the step, time-of-flight spent by the step, etc.). Information given through the B4Step object.
- **Trajectory.** It's the record of a track history. It stores some information of all steps done by the track as objects of B4TrajectoryPoint class.
- **Manager Classes.** Although, Geant 4 is based in C++, and manager classes could be considered to violate the concept of Object-oriented programming, including these classes is a design choice to localize responsibilities and for granular categorization. We may then find several of these classes in any program and more can be created by the user based on their needs.

A key virtual method in the Geant4 package is found in the B4DetectorConstruction. Here, a virtual method called "Construct()" gives access to the construction/definition of all necessary materials, the volume of the detector geometry and it is related to other detector classes.

Once the geometry, the world volume, particles, material, etc. have been created, the whole program is compiled and then it can be ran from the terminal using either of the following commands:

$$./exampleB4 [-m macro] \quad (3.1)$$

$$./exampleB4 [-u UIsession] \quad (3.2)$$

$$./exampleB4 [-t nThreads] \quad (3.3)$$

Option 3.1 uses the -m parameter followed by a macro, this command is usu-

ally used to record the simulated events in .out and .root files. Here we are executing the program in the 'batch' mode and without visualization. After the -m command we include a .in file 3.1 with information about the particle, its energy, the number of events to reproduce and characteristics such if the particle has multi-scattering or not; the data from each step of the simulation is recorded in a .out file with a given name and once the events have finished been run it automatically generates a B4.root file to be analysed. The simulations presented on this thesis have been, in its majority, recreated through this method.

```
[mbramos@phi Geant4]$ cd B4-build/B4a  
[mbramos@phi B4a]$ ./exampleB4a -m electron_100GeV.in > ele_100GeV.out
```

Figure 3.1: Code use in Geant4 to simulate an incoming particle based on the characteristics described in the .in file (here representing an electron at 100 GeV).

The result from running the software this way, as mentioned, would result in the creation of a ROOT file containing the data of the simulation and which can be analysed using software macros written in C++ or Python. ROOT, like Geant4, is a modular scientific software toolkit developed at CERN, it includes all functionalities needed to deal with big data processing, statistical analysis, visualization and storage [2].

Option 3.2 introduces an interactive mode with the -u command, following -u we would include any selected UI session of our choice like tcsh to interact with the interface of the program. Allowing us to create visualizations in 3D of the detector/calorimeter.

Finally, option 3.3, presents the -t command which is only available in multi-threading mode (which is the mode we have run in this project) and it allows the

user to override the Geant4 default number of threads. This method can be used for either 3.1 or 3.2 and allows us to run across more cores.

To run this visualizations in this thesis, we have used method 3.3 assigning the number of nThreads to 1, and then we follow the next 4 commands from 3.4 to 3.7:

$$\textit{/run/initialize} \tag{3.4}$$

$$\textit{/gun/particle/ e-} \tag{3.5}$$

$$\textit{/gun/energy 100 GeV} \tag{3.6}$$

$$\textit{/run/beamOn 1} \tag{3.7}$$

As described previously on the basics, here we are giving our program the orders it needs to run, we initialise it (3.4), then we assign the particle we want to inject in the detector, an electron in our example above (3.5) although muons, photons, positrons or others are also programmed options; the energy of the injected particle is also given (3.6). Finally it is possible to activate the beam defining the number of times we want to repeat the process. When running in the visualisation mode, one event/run is considered for each visualisation (3.7). An example of a visualization of how the result would look is presented in figures 3.2a and 3.2b, where an electron at 100 GeV enters a calorimeter of 4 modules.

Two calorimeter designs have been studied in this project: a simple one, where the calorimeter is composed of one simple module; and a more complex but realistic one, where the calorimeter is made of 4 modules separated by gaps. The two designs as well as the studied materials are given in the following sections.

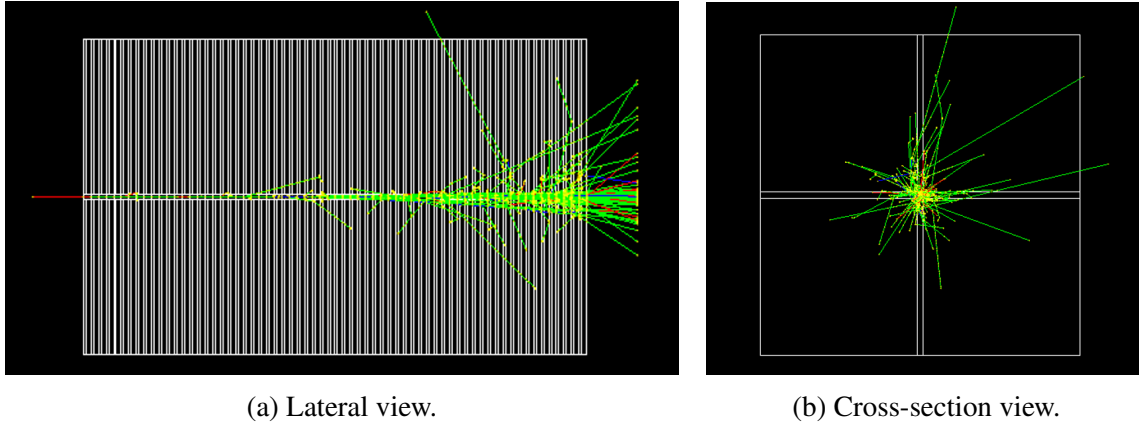


Figure 3.2: In green and entering the calorimeter from left to right (a) is an electron at 100 GeV accessing the calorimeter with coordinates (0, 0) and creating a shower, a view of the cross-section is also presented (b).

## 3.2 A simple calorimeter Layout

The so-called “simple” calorimeter layout is based of Geant4’s example B4 [31] and is the one used to set the physics background on a wide part of this research because of its one sector calorimeter design.

This single module calorimeter has been designed considering 66 layers of interleaved 4 mm plastic scintillators and 2mm lead absorber plates, with a square cross-section (surface) covering 12.1 x 12.1 cm. A visual sketch of how each layer is divided in gaps and absorbers can be see in the following figure 3.3.

This simple design only considers 1 module, if we were to take the previous figure 3.2b as reference, we would only see one of the differentiated squares rather than all four. For the tests showed in the next chapter, particles are injected in the centre of the single module. Under these conditions, the highest possible amount of energy will be deposited as it maximises the probability that the shower is contained in one module, figure 3.4.

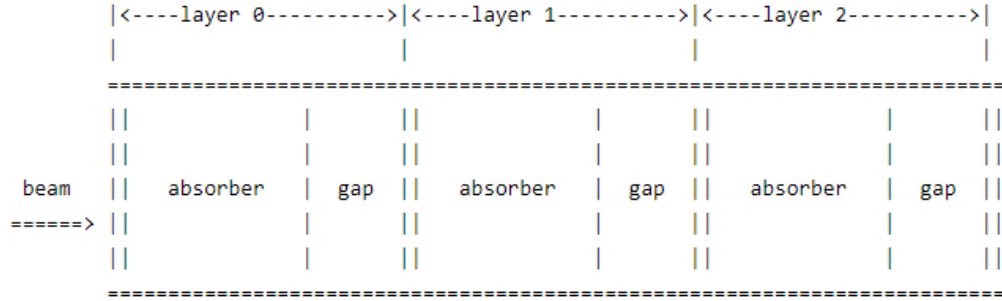


Figure 3.3: Sketch of the first three layers (from 0 to 2) for a single module calorimeter. Each layer shows how it is divided in absorbers and gaps which are then used to record the energy deposit of the particles.

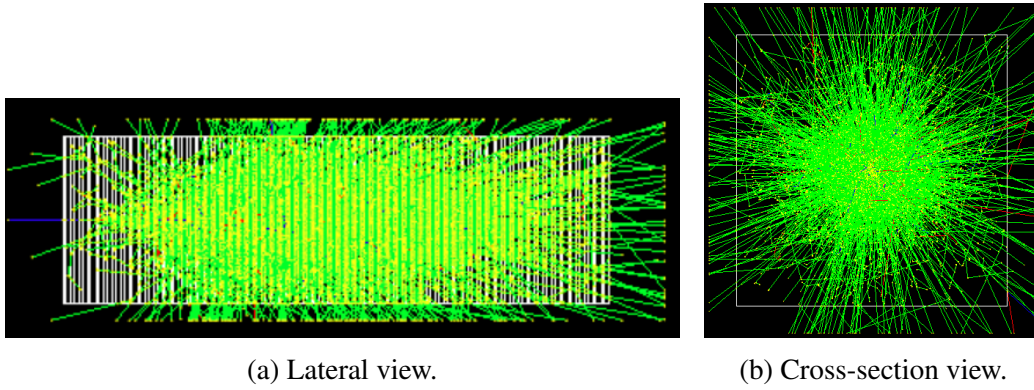
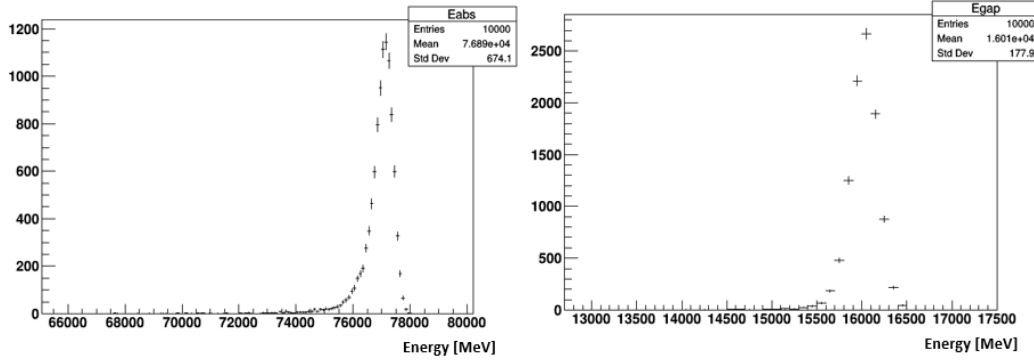


Figure 3.4: Cross-section of a single module calorimeter, defined with the white line square, showing the deposited energy of a simulated electron of 1 TeV accessing the calorimeter with coordinates (0, 0). Showers shown in green.

For each simulation performed, Geant4 lets you visualise it as shown on figure 3.4 and also provides root files for deeper analysis as explained at the beginning of this chapter. The next figures presents individually the distribution of the energy deposited in the absorber, 3.5a, and in the gap, 3.5b, for incident 100 GeV electrons. A higher amount of energy is deposited in the absorber, around a 77% of the total energy of the particle while the energy deposit on the gap is around

16% of the total injected energy.

Only the energy deposited in the gap can be read out by the calorimeter read out system, on the other hand the absorber energy is the fraction of energy "lost". Detailed studies of these quantities for various energy values and particle types will be presented in the next chapter.



(a) Energy deposit in absorber.

(b) Energy deposit in gap.

Figure 3.5: The energy deposits of an electron of 100 GeV are shown in these two figures which share a negative-skewed like distribution. (a) shows the energy deposited in the absorber and (b) the energy on the gap. The X axis shows the energy in MeV and the Y axis the number of events.

### 3.3 A more realistic layout

Once we have understood how to work with Geant4 and the response of the material to particles, we have implemented a more realistic version of the layout. This section describes the geometry and Geant4 implementation.

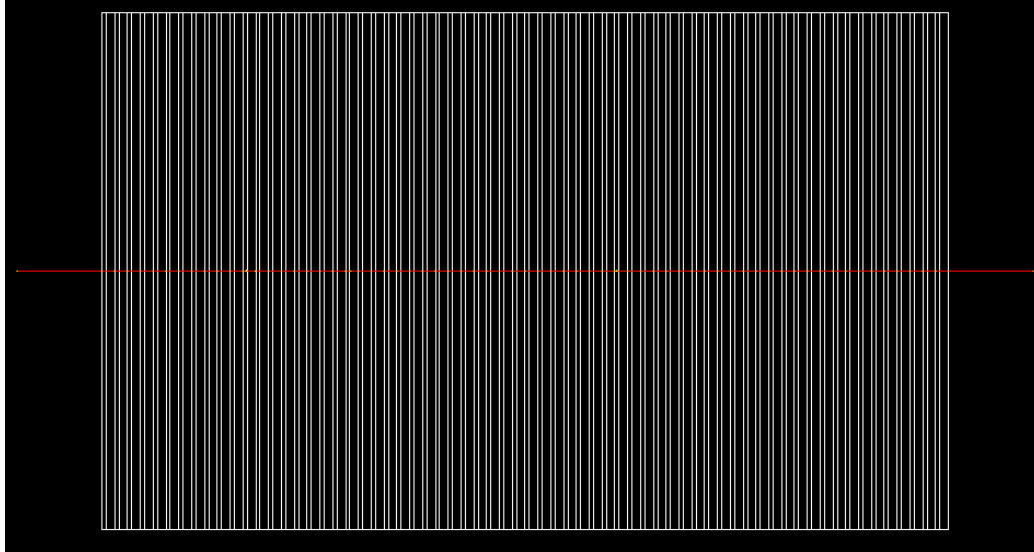
In this design we keep the 66 layers mentioned previously but change the single module for a four module calorimeter with asymmetric gaps between them. The X axis gap is 0.2 mm thick and the Y axis gap is 1.2 mm, detailed in figure

3.6b. This gap between modules is filled fully with air in the simulations although a thin panel of stainless steel surrounding each module has been added in some simulations too for research and comparison as it is expected to be present in the final design.

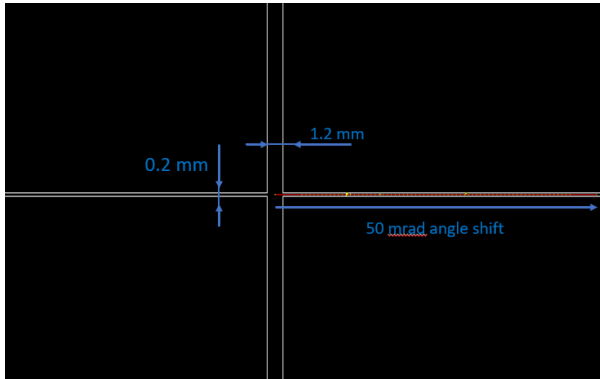
A key difference with the designs shown previously is that for this layout, we consider the calorimeter to be tilted with respect to the beam by 50 mrad. This tilt should be expected on FASER after installing it in TI12 so, to emulate this condition, we have stated that the beams will access the calorimeter with a shift angle of 50 mrad in the positive X axis.

Because of the new characteristics added to the design, if we inject a particle with entrance coordinates at (0, 0), as we have been showing so far, now the entrance trajectory of the particle would be tilted by 50 mrad from the origin coordinates. Also, as we are using air in the gap, having a low density of  $0.0013 \text{ g/cm}^3$ , we should expect that if a beam does not interact with the material of the module but instead stays only in the gap (as it happens with (0, 0) entrance coordinates), see figures 3.6, it will experience a very low energy loss and no showers as opposed to when it gets into contact with the modules (as it should happen with other coordinate combinations like (10, -10)).

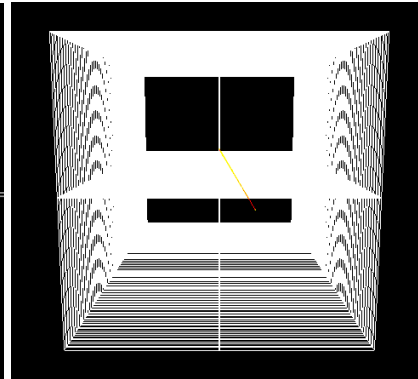
Studies on this are reported in Chapter 4.



(a) Lateral view.



(b) Cross-section zoomed in.



(c) Frontal depth view.

Figure 3.6: Three different views of the realistic layout with an electron of 100 GeV accessing the calorimeter at entrance coordinates of (0, 0) and a shift on the angle of 50 mrad. The first figure (a) provides a better look at the centered entrance of the particle, represented in red. As the particle moves through the air gap between modules it does not generate showers. Figure (b) presents with annotations the angle shift and the size of the gap. A better look at the trajectory of the particle due to the shift angle is shown in the third figure (c).



### 3.4 Material dependence and multiple scattering

To illustrate the relevance of considering realistic physics effects related to particles passing through material, and dependence of the particle response to different material, we have performed tests switching on and off the presence of multiple scattering and changing the interactive medium. Details on the form of the distributions and the fit functions that can be used to interpret the results will be explained in the next chapter.

**Multi-Scattering:** as particles move through matter they undergo repeated elastic Coulomb scattering. In an ideal scenario, this scattering would be single (no multi-scattering). This would happen assuming that the thickness of the material it interacts with is extremely small, one localized scattering center, so then, the probability to have more than one interaction is negligible. But in real-life experiments with solid state detectors like the one used for FASER, the thickness of the material is increased so the number of interactions becomes high and tends to generate showers of particles [62].

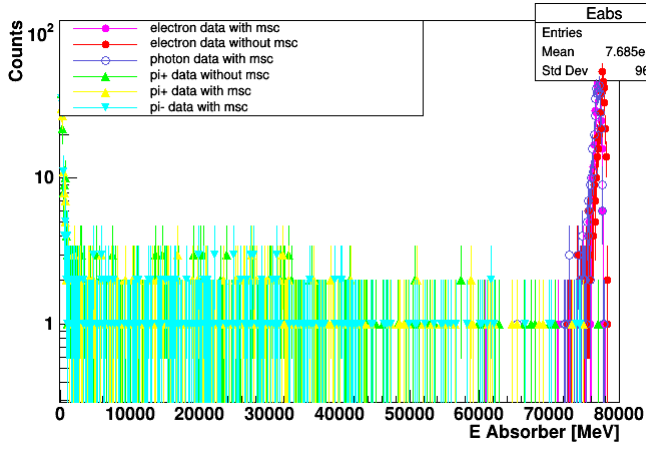
While we expect to record multiple scattering in FASER, it is wise to study how these two types of scattering compare to each other to differentiate real-world data (multi-scattering or msc) with ideal case situations (no multi-scattering or nomsc). This experimental analysis is described in more detail in the next chapter and shown in figures 4.7, 4.5a and 4.5b; where we can observe how during multi-scattering particles spread more showers and lead to an increase of energy deposited in the calorimeter.

**Material dependence:** To expand the research, and making the most out of the options from Geant4, a study comparing the reaction of particles with two different materials used on the modules of the calorimeter has been developed. The

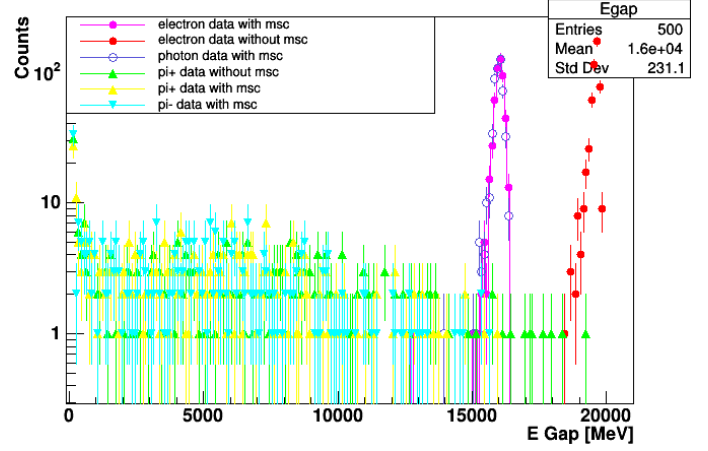
particles used in the study include electrons,  $e^-$ , photons,  $\gamma$ , and pions,  $\pi^+$  and  $\pi^-$ , where  $e^-$  and  $\pi^+$  data has been generated with and without multi-scattering. Following the deposited energy analysis introduced at the end of section 3.2, we have studied how all these particles compare to each other as they are introduced through a plastic calorimeter (like in FASER) studying individually their response on the absorber, figure 3.7a and on the gap, figure 3.7b. Also, we repeated this study for a Liquid Argon calorimeter (like in ATLAS) to compare responses, figures 3.7c (absorber data) and 3.7d (gap data).

Particles on the right hand side present a negative-skewed distribution with short tails (they interact heavily with the material) while particles on the left hand side show a positive-skewed distribution with low and long tails (they do not interact heavily with the material and leave the detector quicker).

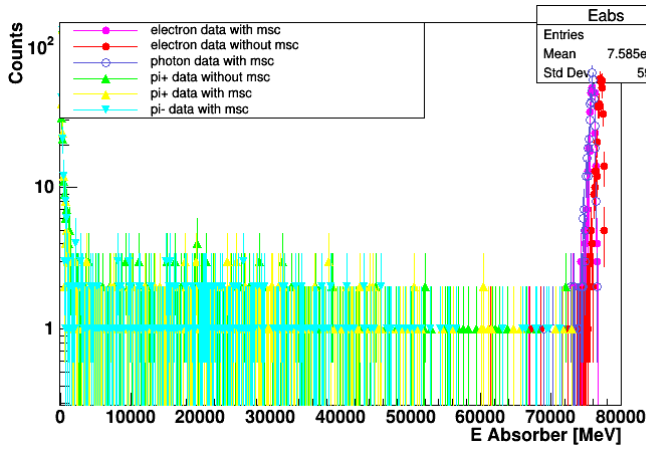
In the design used in the calorimeter of FASER, the collaboration settled for the use of plastic calorimeters as these are being re-used from the LHCb experiment. From these figures we can observe a similar response on the Liquid Argon calorimeter and the plastic calorimeter, figure 3.7. Despite the fact that the Liquid Argon calorimeter records a higher fraction of energy, because of economic costs the Plastic calorimeter was chosen instead.



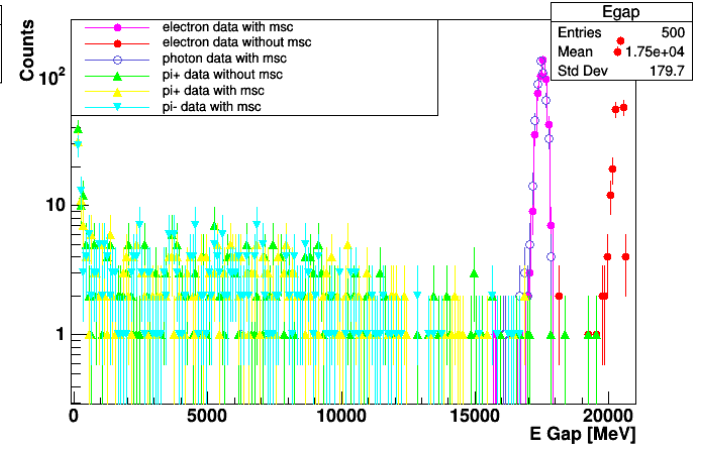
(a) Energy deposit in absorber of Plastic detector.



(b) Energy deposit in gap of Plastic detector.



(c) Energy deposit in absorber of Liquid Argon detector.



(d) Energy deposit in gap of Liquid Argon detector.

Figure 3.7: Data of photons (light purple), anti-Pions (cyan), Pions with msc (yellow), Pions without msc (Green) and electrons with msc (solid pink) and without multi-scattering (red), all at 100 GeV, depositing energy on the absorbers (a, c) and gaps (b, d) of two different calorimeters. The first line (a, b) refers to a plastic calorimeter and the bottom line (c, d) refers to a calorimeter made out of liquid argon, both based on the single module configuration. A logarithmic scale has been used in the Y axis.

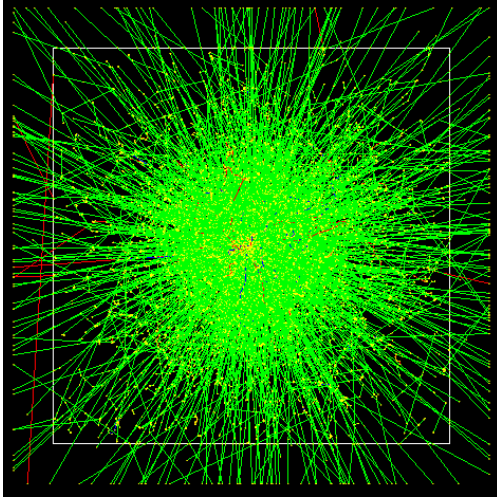
## 3.5 Simulated data

We will use Geant4 to simulate the samples needed to perform the following studies presented in chapters 4 and 5:

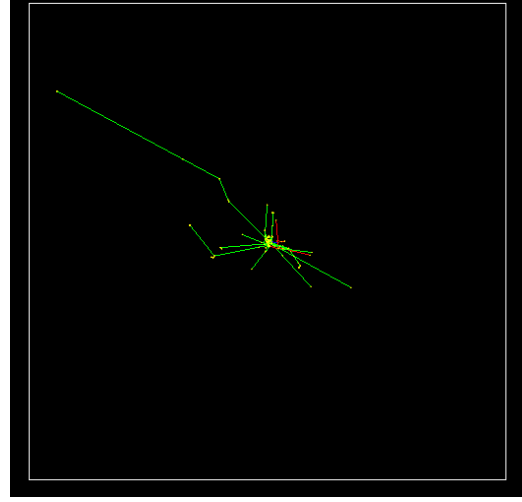
- **Electrons and photons with different injected energies, as well as pions.**
- **Electrons at different injection angles .**
- **Muons with different injected energies.**

Electrons and photons generate complex showers within the electromagnetic calorimeter, hence their generation time is the higher than the one for muons. At the same time, particles with higher energies (TeV range) will also take longer to be generated than particles in lower energy ranges (GeV range).

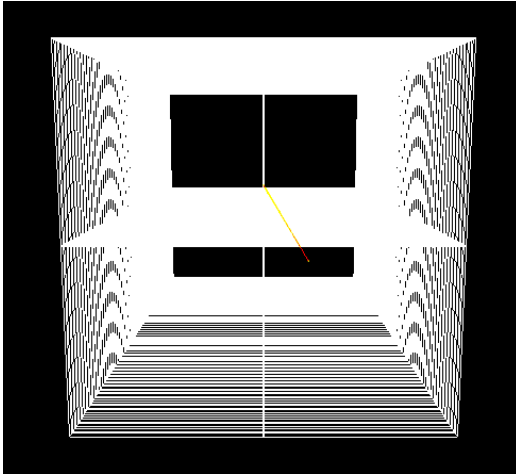
This situation can be observed in the following table 3.1, which shows the approximate time required to generate any file as a function of the energy of the particle considered. This is shown for electrons (which will provide similar results to the photons) and muons. Electrons generate complex showers when interacting with the modules of the calorimeter while muons exit the calorimeter fast without losing much energy 3.8. Taking into account the presence of the air gap between the modules, when particles move past it without interacting with the material of the modules then they will exit the calorimeter quickly and without generating showers regardless of their charge.



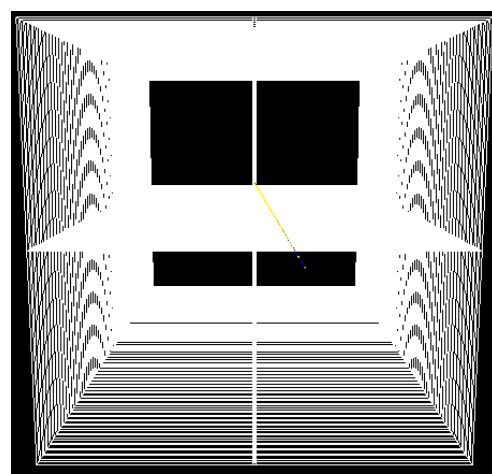
(a) Electron in simple calorimeter.



(b) Muon in simple calorimeter.



(c) Electron in realistic calorimeter.



(d) Muon in realistic calorimeter.

Figure 3.8: Two case scenarios expected when running simulations, created with entrance coordinates at origin  $(0, 0)$  at 100 GeV. The top layer shows the showers of electrons (a) and muons (b) interacting with the material of a single module calorimeter. On the bottom layer simulations are performed on the more realistic layout, particles moving across the air gap and not interacting with the material of the module deposit a small amount of energy and create small or non-existent showers. Electrons (c) and muons (d) (shown with a depth perspective).

<b>Time per simulation based on energy and material interaction</b>	
Energy of particles	Time per event simulated
100 GeV - gap-electrons or muons	< 1 sec
100 GeV - head-on electrons	3.6 sec
1TeV - gap-electrons or muons	<~ 1 sec
1TeV - head-on electrons	26.5 sec

Table 3.1: An approximate comparison on how long it takes to generate files for electrons and muons based on their incoming energy and on how much they interact with the material of the module. Files for photons would share the same timing as electrons.

These timings have been obtained from measuring how long it takes to generate a single file of simulated data divided by the number of events simulated in each file. In a wide part of this thesis, the data used comes from simulations of 10,000 events for each particle although, based on the time constrains, the simulations performed on the new calorimeter layout have been performed for 500 events per file instead.

## **Chapter 4**

# **Simulated data analysis: electrons and photons**

During this research thesis, a series of simulations have been generated to test the response of FASER's calorimeter to incoming charged particles. As a result, we can analyse these responses and the studies around them are presented over the next two chapters.

In this chapter the energy loss of electrons and photons are studied in different manners, also the entrance angle of electrons has been examined thoroughly to understand the deposited energy dependence for changing entrance angles.

First, simulations generated using the single module calorimeter layout are presented and then those generated from the more realistic layout featuring the four module design.

## 4.1 Data analysis description

The main signal FASER's calorimeter targets is that of the electrons so many of the studies performed in this section are on the electron's response. A typical response from this particle can be shown to fit a Gaussian distribution around the mean counting with power law tails as can be seen from the explanations shown in this section.

The center of the distribution of energy deposits can be represented with a **Gaussian distribution** following the characteristics of image 4.1:

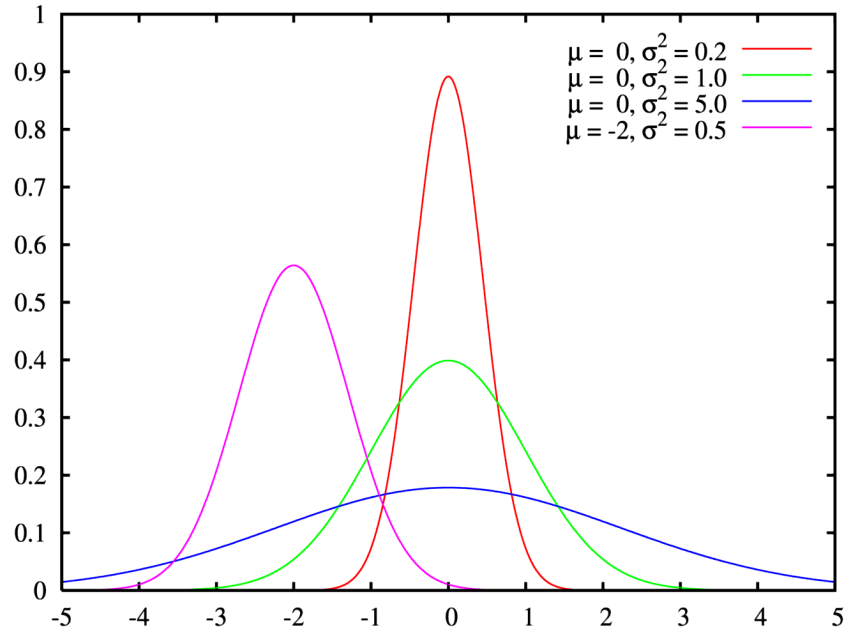


Figure 4.1: Gaussian distribution for 3 different combinations of parameters.

This function is described by the equation:

$$P(x) = \frac{1}{\sigma\sqrt{2\pi}} e^{-(x-\mu)^2/2\sigma^2} \quad (4.1)$$



where  $\mu$  is the mean of the distribution and  $\sigma^2$  is the variance.

While this Gaussian fit only uses two parameters to designate the distribution, a more complete function to fit the distribution of the energy deposited by the particle, like those shown in figures 4.5a (for the absorber) and 4.5b (for the gap) in the next section, would be the **Crystal Ball** which is described by the following equation 4.2 needed to generate the distribution in figure 4.2:

$$f(x; \alpha, n, \bar{x}, \sigma) = N \cdot \begin{cases} \exp(-\frac{(x-\bar{x})^2}{2\sigma^2}), & \text{for } \frac{x-\bar{x}}{\sigma} > -\alpha \\ A \cdot (B - \frac{x-\bar{x}}{\sigma})^{-n}, & \text{for } \frac{x-\bar{x}}{\sigma} \leq -\alpha \end{cases} \quad (4.2)$$

where:

$$A = (\frac{n}{|\alpha|})^n \cdot \exp(-\frac{|\alpha|^2}{2}) \quad \text{and} \quad B = \frac{n}{|\alpha|} - |\alpha| \quad (4.3)$$

and the parameters are described as:

1.  $\bar{x}$  = Mean of the Gaussian.
2.  $\sigma$  = Standard deviation of the Gaussian.
3.  $\alpha$  = how many  $\sigma$  away from the mean does the tail start.
4. **n** = Power law tail component.

Because of the increase in parameters provided by the Crystal Ball function compared to the Gaussian fit, which includes the sigma and alpha parameters with additional physical meaning, this function will always provide a better fit in these studies. On the other hand, comparing the mean data of the gap over the initial

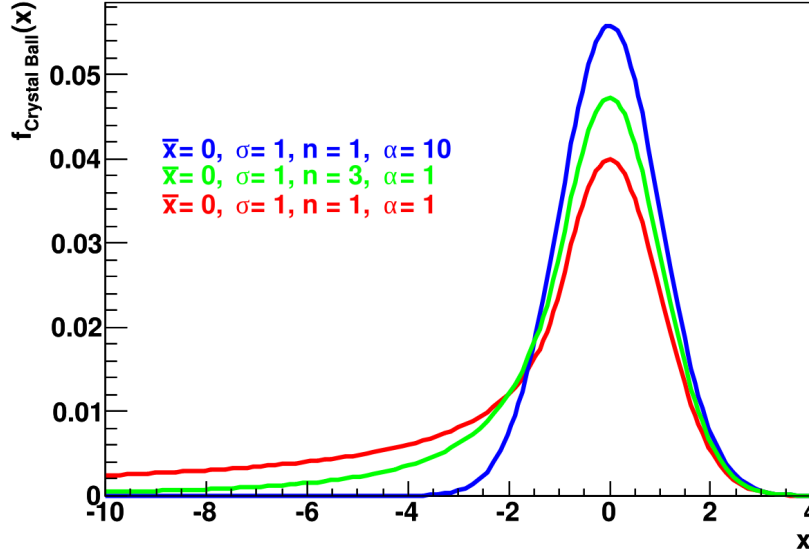


Figure 4.2: Crystal Ball distribution with 3 different combinations of the parameters.

energy for the Crystal Ball fit and the Gaussian fit, we can see in figure 4.3 that the means of Gaussian and Crystal Ball fits are similar. We also see a slight decrease in mean with injected energy due to "punch through", the effect where a significant amount of energy goes over the calorimeter's length.

Based on these figures, we should expect a similar result on our studies if we apply either the Gaussian or the Crystal Ball fit.

An additional study analysing the physics impact of the parameters of the Crystal Ball is also presented, figure 4.4:

We studied the sigma over mean gap energy, as shown in figure 4.4a. An increase for initial energy above 100 GeV, due to a significant "punch through" can be observed.

Figure 4.4b then shows that alpha value of the crystal ball, which gives information about the characteristics of the tails. Smaller values of alpha means higher

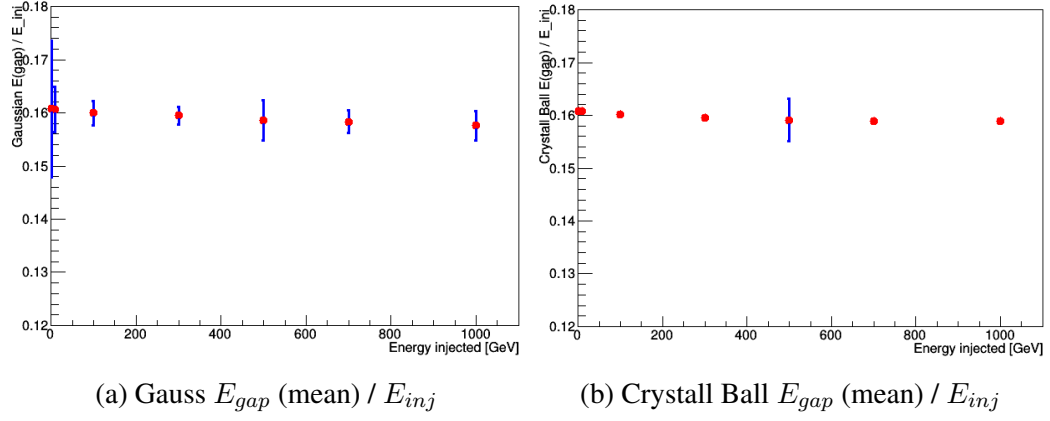


Figure 4.3: Studies comparing the Energy Gap mean using a Gaussian and a Crystal Ball fit.

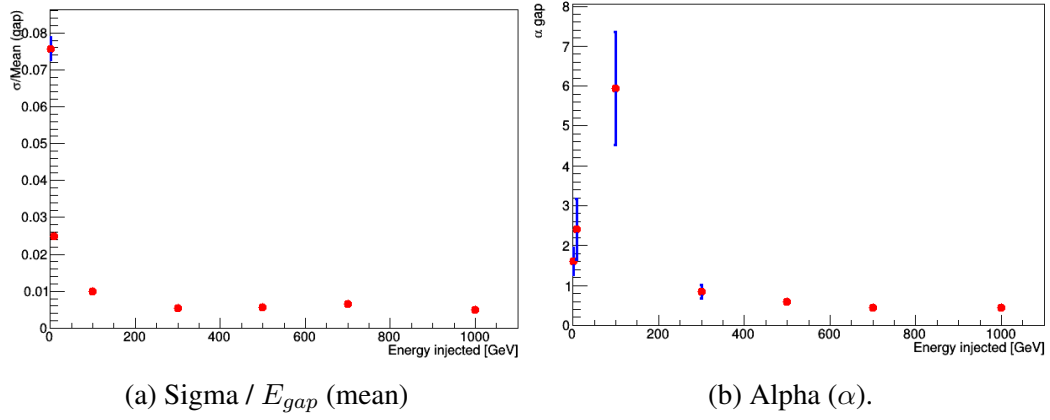


Figure 4.4: Studies on the sigma over  $E_{gap}$  mean and the alpha parameters using the Crystal Ball function.

tails in the energy (higher losses), which is evident at energies above 100 GeV.

The details of the Crystal Ball fits have been worked out in collaboration with the other member of the team and described in that report. Here we show the results of the fit and the study of the main parameter.

## 4.2 Analysis for electrons

As electrons and photons interact with a material (via QED processes), for energies above 10 MeV the main source of electron energy loss is bremsstrahlung and interactions between photons produce mainly  $e^+ e^-$  pairs. At energies above 1 GeV these processes become more energy independent and we should expect electrons and photons producing secondary photons via bremsstrahlung or producing secondary electrons and positrons by pair production. These secondary particles will then implement the same mechanisms producing other particles and hence, generating a shower which degrades progressively [35].

### 4.2.1 Energy deposit

Using this physics background we can use Geant4 to study the energy deposit of electrons moving across the calorimeter. With this software, we can simulate particles travelling through the absorber and gap components of the calorimeter to investigate how at different energies, these particles show different losses across the detector. When making energy deposit studies, it is important to consider that ideally, if the calorimeter was keeping all the energy  $E_{gap} + E_{abs}$  would equal the injected energy but, in real world conditions  $E_{gap} + E_{abs}$  is always smaller than the total injected energy because of energy losses.

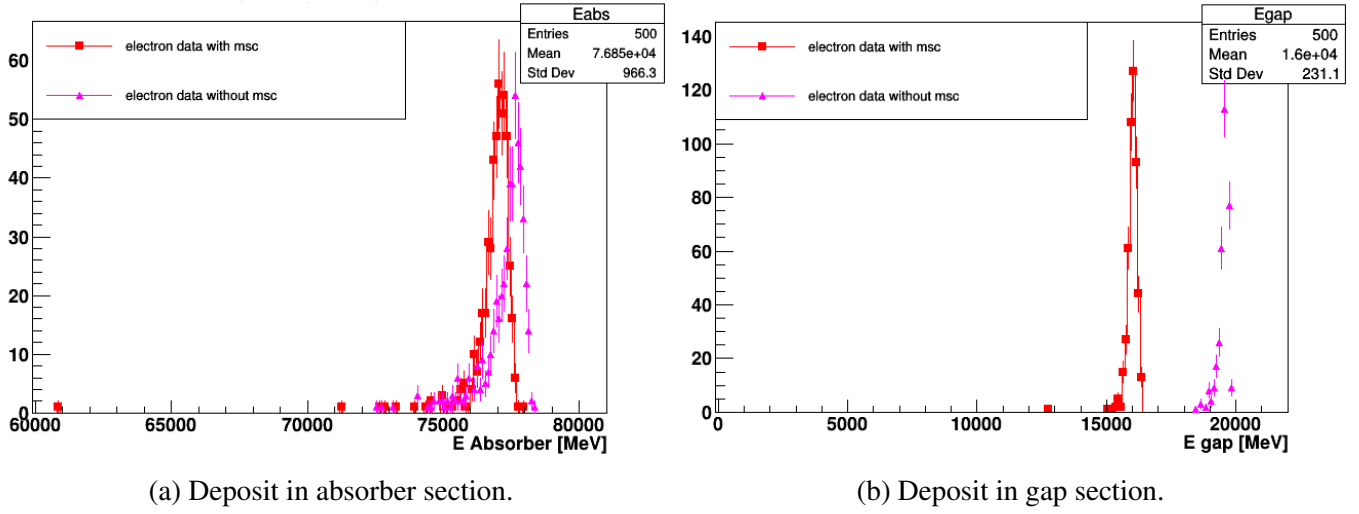
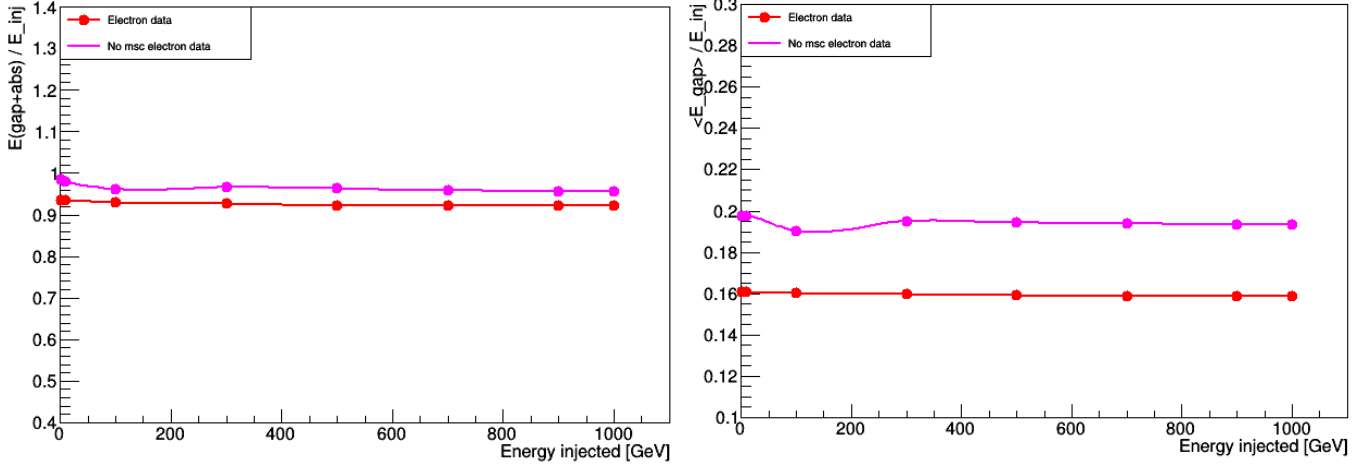


Figure 4.5: Simulation of a 100 GeV electron across the calorimeter, energy versus number of events. In the left (a), energy is deposited in the absorber, the energy released by particles undergoing msc is close to the one released by optimal particles without msc. On the right (b), is the energy deposited on the gap, differences between msc and no msc place the energy peaks almost 4000 MeV apart.

Another factor that will impact the amount of energy deposited by any given particle in the calorimeter is the presence or not of multi-scattering (msc) as described in section 3.4, and the analysis covering these characteristics is presented in this section.

In figure 4.5, a study simulating electrons with and without msc. Here we present electrons at 100 GeV depositing energies in different proportions in the absorber, figure 4.5a, and in the gap, figure 4.5b, where the differences between applying multi-scattering and not applying it are distinguished. Here, we can also observe the distributions we discussed in the previous section 4.2, observing a Gaussian fit in the mean but which could be better described using the Crystal Ball fit.

Then, using the Crystal Ball fit we present the resulting fraction of deposited energies for the total deposited energy, figure 4.6a, and the energy deposited in



(a) Toal energy fraction.

(b) Gap energy fraction.

Figure 4.6: Using a crystal ball fit, this figure shows the fraction of energy deposited as a function of injected energy. The graphs present data from electrons with msc (Red) and without msc (Pink). An over-fit can be expected at 100 GeV with no msc electron data.

the gap, figure 4.6b, as FASER will ultimately use this one as readout for energy deposits. The electron energies used for this study are: 1 GeV, 10 GeV, 100 GeV, 300 GeV, 500 GeV, 700 GeV, 900 GeV and 1 TeV. The fraction of deposited energy is represented by equation 4.2 where the energy deposited in the gap and absorber are added together and divided by the injected energy.

$$\frac{(E_{gap} + E_{abs})}{E_{inj}} \quad (4.4)$$

In this analysis we can study two different features. On the one hand we observe how the electrons with and without msc differ, showing a higher fraction recorded by the data without multi-scattering since this one would carry a smaller amount of energy losses due to showers as compared with the results from electrons with msc which lay below in the graphs. On the other hand, we are also

comparing the fraction of energy deposited as a function of injected energy where we can start to appreciate a small decreasing tendency as the injected energy increases because of the energy losses. The fraction shown in the gap, figure 4.6b, better describes this phenomena as this is the read out data recorded by FASER's calorimeter.

As we were explaining at the beginning of section 4.1, both electrons and photons generate complex showers when they interact with the material of the module/s of a calorimeter and because of this we expect a similar may response as they encounter these modules with different energies. To study how electrons and photons compare we studied their total fraction of energy deposits as a function of injected energy, figure 4.7. Here we are subtracting the total energy to the injected energy before dividing it by injected energy again. As particles move higher in the X axis we expect an increased number of energy losses due to the heaviness of the particles.

From this figure we can conclude that electrons and photons are expected to deposit similar amounts of energy in the modules of the calorimeter.

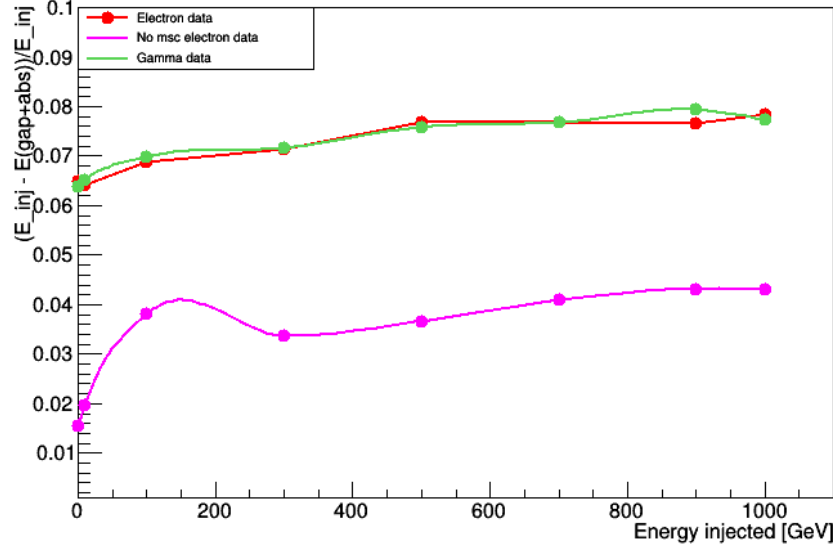


Figure 4.7: Using a crystal ball fit, this figure shows the injected energy minus the sum of energy recorded by the gap and absorber, divided by the injected energy. The graph presents data from photons (Green) and electrons with multi-scattering (Red) and without multi-scattering (Pink). An expected overfit can be expected at 100 GeV with no multi-scattering.

#### 4.2.2 Angular scan in simple layout

From simple particle kinematics [46], we expect different pairs of particles coming from a possible decay of a Dark Photon to enter FASER with different entrance angles. These produced pairs then change the original trajectory of their mother particle as seen on figure 4.8, where there is a mother particle, the Dark Photon, decaying into a  $e^+ - e^-$  pair reaching the calorimeter at different points.

This is specially important to study to better understand the energy losses, which vary depending on the entrance angle into the detector, and is key to reconstruct the incoming pairs of particles and their mother particle accordingly.

While the entering particles access the detector at angles farther apart from the center of the calorimeter (remember that this study considers an "optimal"



configuration with a single module calorimeter as explained in this section and a more realistic configuration with a 4 module configuration, explained in the following section), these particles are likely to leave the detector before reaching its end should the angle be too big. The best candidates should then be electrons accessing FASER at an optimal angle range, still to be determined, where they are most likely to go through the totality of the detector until the end of calorimeter and not leaving the machine half-way through.

This angular dependence can be appreciated in figure 4.8 and is described on chapter 2, which also provides information on the type of particle analysed after registering the energy losses and undergoing reconstruction.

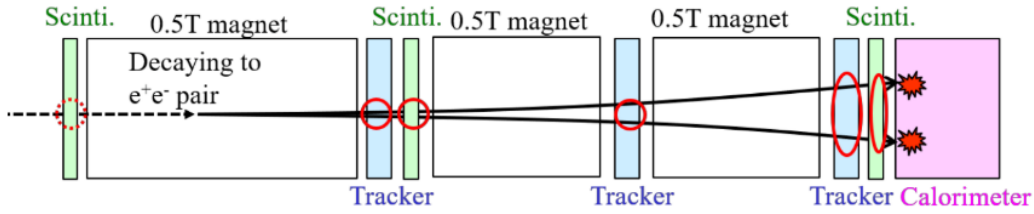


Figure 4.8: Here [6], a pair electron-positron decaying from a Dark Photon is described showing an increasing angle aperture between the pair. We can expect for increasing entrance angles, that pairs have the risk of leaving the detector before reaching the calorimeter or the end of it.

The angular scan analysis is a key component on this thesis. We started studying the energy deposit of 100 GeV electrons as they access the single module layout detector at different entrance angles in a range from 0 to 100 mrad. The fraction of energy deposited in the gap is shown in figure 4.9, with figure 4.9b presenting a zoomed version of figure 4.9a to better depict the differences.

Observing the results we can conclude that for this ideal case, the energy deposited for particles entering up to 15-20 mrad (5 degrees) is constant as a func-

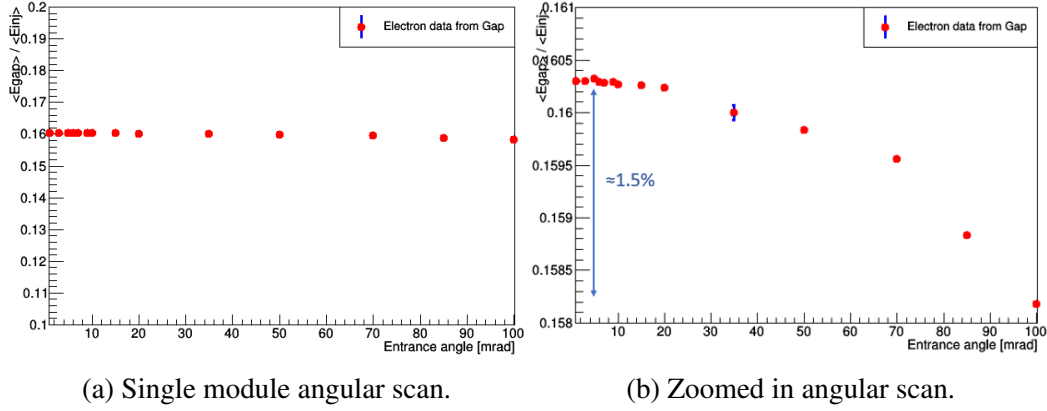


Figure 4.9: Angular scan on ideal calorimeter using a crystal ball fit with entrance coordinates (0, 0). From 0 mrad to 100 mrad angle shift there is approx. 1.5% deviation in energy deposited.

tion of the angle and it decreases only at large angles. This is noticeably important because the opening angle of Dark Photons is expected to be, at maximum, up to 5 degrees.

### 4.2.3 Angular Scan in the more realistic layout

One key difference between the original and current configurations that impacts the results presented on this study include, apart from the already mentioned differences in structure of the calorimeter, a newly added shift angle of 50 mrad, as described in section 3.2, that make the beam get to the back face of the detector with an offset as the calorimeter is tilted with relation to the beam line to prevent particles from going straight through the gap and not being efficiently recorded.

The angular scan generated for the current configuration covers the range from -100 mrad to 100 mrad across the X axis, since we are incorporating a 50 mrad shift angle, also in X axis, we will no longer obtain a symmetric response as would

have happened in the previous section.

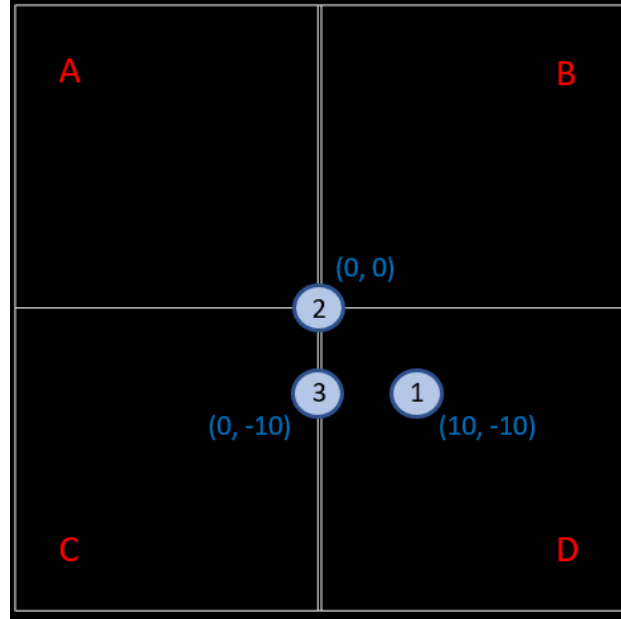


Figure 4.10: Presents the coordinates studied in this thesis, numbered in order, for the three cases described in this section. Also orders alphabetically the 4 modules of the calorimeter.

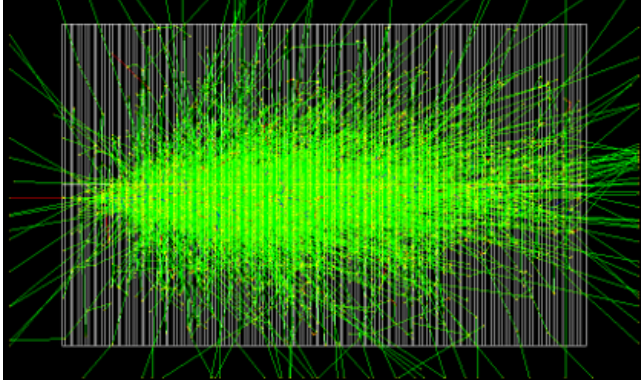
Hence, the more realistic configuration generates a different angular scan and we have identified three key situations to study in this section, as illustrated in figure 4.10.

1. **(10, -10) coordinates** Angular scan for a particle incident on one of the 4 modules.
2. **(0, 0) coordinates:** Angular scan for a particle incident in the centre of the calorimeter (centre of the gap).
3. **(0, -10) coordinates:** Angular scan for a particle incident along the gap.

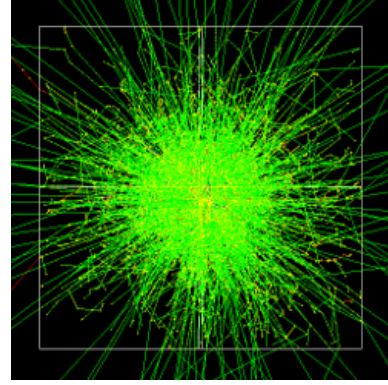
### 1. (10, -10) coordinates.

Here we simulate particles with an entrance position 10 mm away in the X and Y axis from the origin. As this position places the beam closer to the centre of the module we should expect a similar response on the fraction of energy lost, to that observed in the previous section (from 0 mrad to 100 mrad) despite the clear differences in design. As we cover a wider range now, and always remembering the presence of a shift angle of 50 mrad in the X axis, we expect the two extreme angle positions chosen, -100 mrad and 100 mrad to record some of the lowest energies deposited. The -100 mrad simulation generates the center of the beam moving close to the inner edge of module C, so a part of the shower is lost in the gap and cannot be recorded as deposited energy, while the 100 mrad simulation places the center of the beam closer to the outer edge of module D, see figure 4.11.

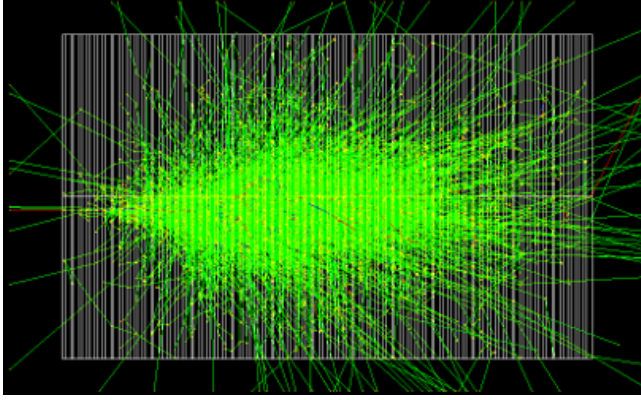
The full angular scan is presented in figure 4.12a, where we observe the particle's response for changing angles and we appreciate the lower position of the extremes in the range mentioned above. The fraction of energy deposited in the gap as a function of the angle is also shown in figure 4.12a and 4.12c, where the respective zoomed in figures are shown in 4.12b and 4.12d to visualise that there are differences.



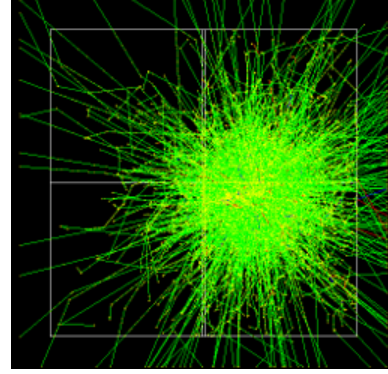
(a) -100 mrad lateral view.



(b) -100 mrad cross-section view.



(c) 100 mrad lateral view.



(d) 100 mrad cross-section view.

Figure 4.11: Case scenarios for the -100 mrad (a, b) and 100 mrad (c, d) of the angular scan showing how the beams move closer to the edges of the modules.

## 2. (0, 0) coordinates.

We are now generating the angular scan across the X axis where we count with an air gap between top and bottom modules of 0.2 mm while the gap between left and right modules is increased to 1.2 mm. As a result, the beam of incoming particles is not directly interacting with the plastic material of any of the modules and hence, no significant shower nor energy deposit is registered. Figure 4.13. As seen on figure 4.14a, we can observe the small fraction of energy deposited if the

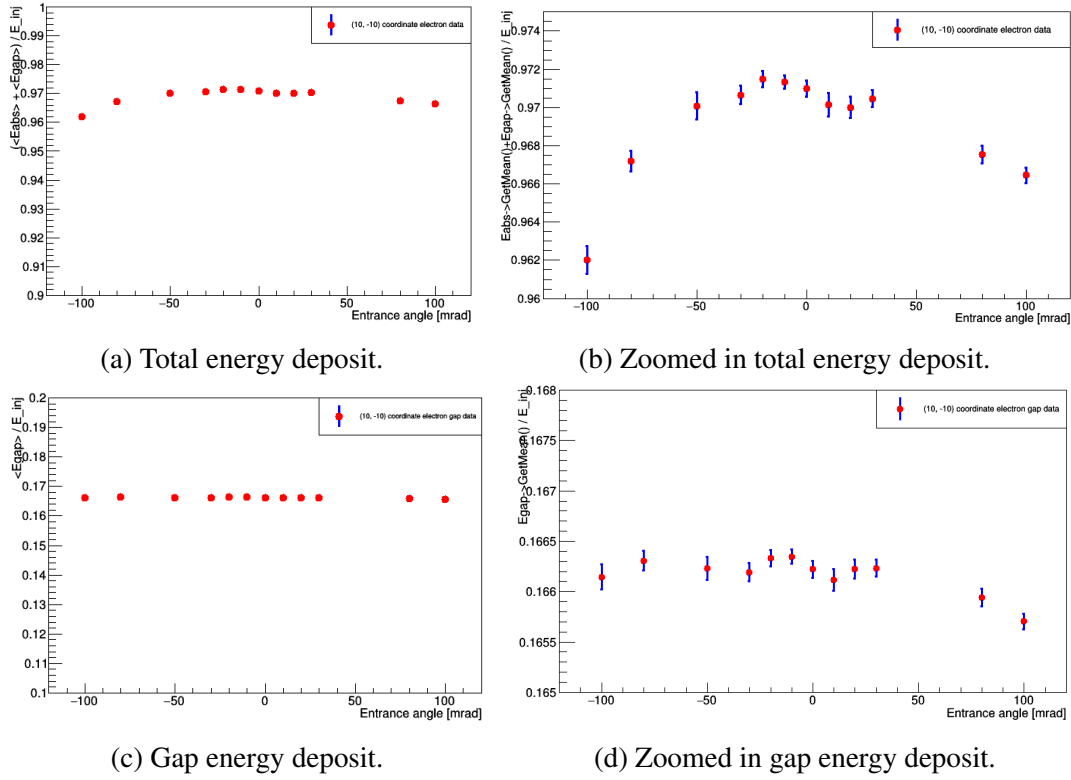


Figure 4.12: Shows the fraction of energy deposited from 100 GeV electrons entering the calorimeter at coordinates (10 mm, -10 mm) and as a function of changing angle. Analysed using the Gaussian mean.

particle moves across the gap, currently on the order of  $10^{-6}$ .

Also, we decided to increase the energy for this study from 100 GeV to 1 TeV, figure 4.14b, to compare different particle's energy response to the angular scan and, even at high energies, we observe no significant changes in deposited energy (no presence of showers). Hence, a particle moving through the gap will maintain trajectory without interacting with the material of the modules regardless of energy.

As the particle does not interact with any module, there is no useful insight from studying the absorber and gap components separately.

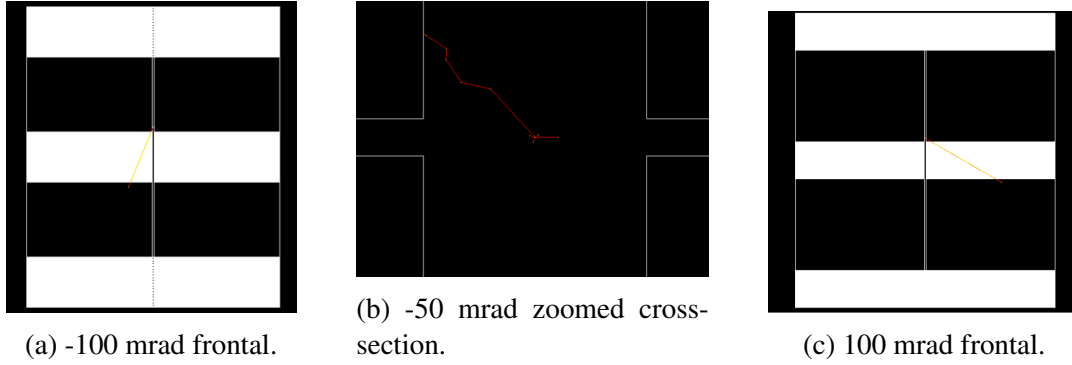


Figure 4.13: Visualizations for 3 different angles in the range studied. (a) shows an entrance angle of -100 mrad, the beam moves across the gap between modules A and C. (b) is a close-up look at a particle with -50 mrad trajectory, compensates the shift angle moves through the centre of the calorimeter. (c) shows an entrance angle of 100 mrad, the beam moves across the gap between module B and D.

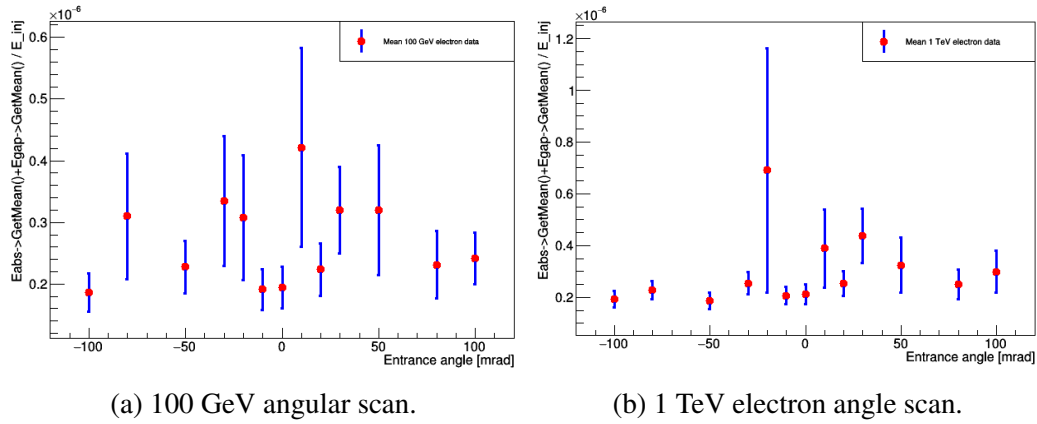


Figure 4.14: Fraction of energy deposited from electrons entering the calorimeter at coordinates (0 mm, 0 mm). Important to notice these figures have been extremely zoomed in as there is a small fraction of deposited energy of the order of  $10^{-6}$ . Both 100 GeV and 1 TeV data can be considered on the same range of impact.

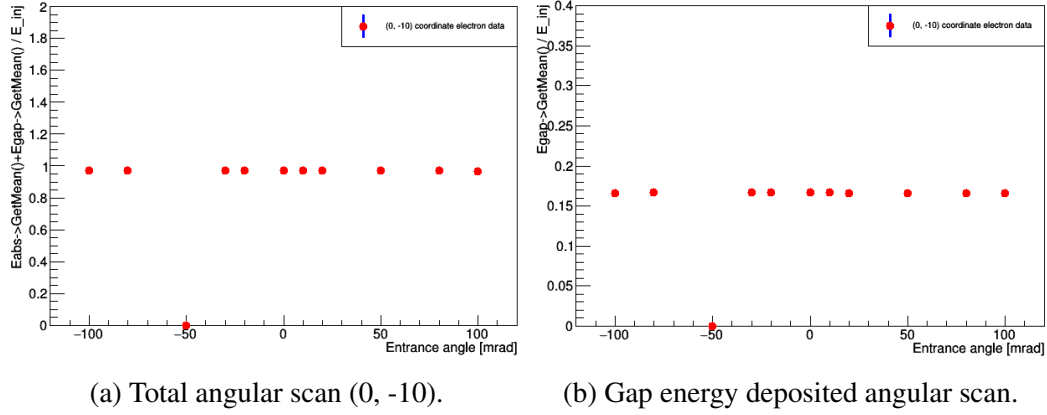


Figure 4.15: Shows the fraction of energy deposited from 100 GeV electrons entering the calorimeter at coordinates (0 mm, -10 mm). (a) shows the total fraction of energy deposited and (b) that of the gap. Errors are too small to be seen.

### 3. (0, -10) coordinates.

This last case-study starts the beam at a 0 mm in the X axis and down 10 mm in the Y axis. Here we will record the lowest energy deposit when the simulation takes an entrance angle of -50 mrad, in this occasion the beam will recover the original 50 mrad shift angle bringing the beam right in the 1.2 mm air gap between module C and D. Figure 4.15 shows the energy fraction dependence over changing angle for the total energy deposited, figure 4.15a, and the energy deposited in the gap, 4.15b. As we can observe, with the resolution of this calorimeter we should expect a constant dependence for changing angle and we encounter a blind spot at -50 mrad. This is because at -50 mrad we are balancing the shift angle of +50 mrad considered in our configuration so now the beam is moving across the gap between modules A and C and is not depositing any energy.

In the next set of figures 4.16, we have generated simulations for incoming beams with different entrance angles: a beam at -100 mrad, a beam at -50 mrad



and at 100 mrad; where we present their cross-section to better understand the data through visualizing events.

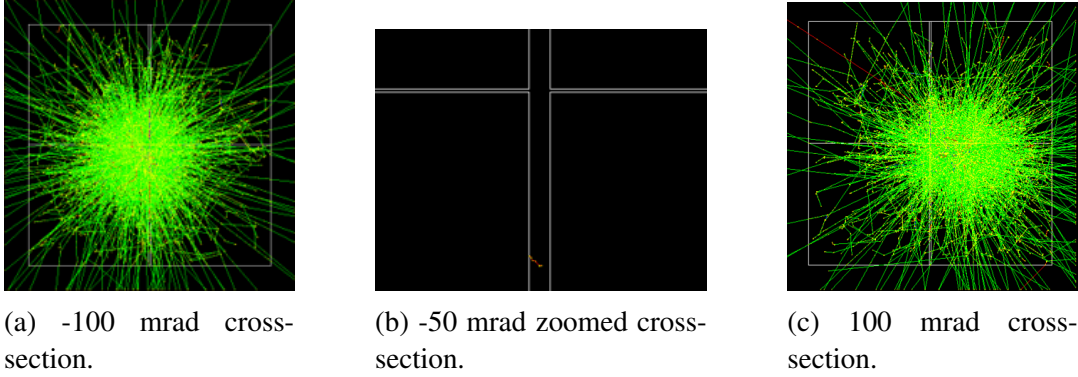


Figure 4.16: 3 different visualizations for 3 different angles in the range studied. In the left (a) we see the shower for a beam with entrance angle -100 mrad with a strong interaction in all modules. In the centre (b), we have a close-up look at a particle with -50 mrad trajectory, this one compensates the shift angle and places the beam right in the 1.2 mm air gap between module C and D. On the right (c) a view at a 100 mrad simulation with a shower interacting mostly in module B and D, but a part of the energy is lost outside the calorimeter or in the gap.

# Chapter 5

## Simulated data analysis: muons and pions

In this chapter different studies performed on the response of muons and pions are presented.

### 5.1 Muon studies

Muons lose energy as they move across objects via ionization, they are minimum ionising particles (MIP) which, above 200 MeV and below 100 GeV, radiate and produce  $e^-$ , known as noise or overflow. While the calorimeter is not used to reconstruct muons (incoming particles such as muons, leaving almost no energy in the ECAL, and hadrons depositing no energy [54]), it is important to understand their behaviour since very energetic muons could mimic signal and be a background for physics analysis. Furthermore, real muons will be used for test beams of the modules and in the future these simulated results can be used for

comparison.

Previously we have seen how electrons have a very short tail. In the case of high energy muons, we should expect a wider area for the peak which leads to tails with a higher amount of events compared to the rest of studied particles. A good visualization of this wider peak is figure 5.4, from the following section.

The fraction of events in the tails is represented by equation 4.2,

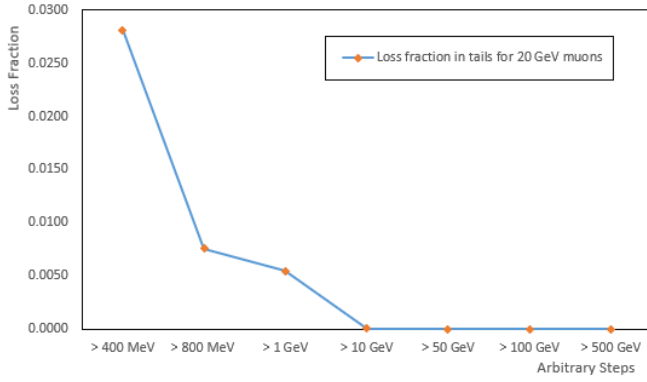
$$FractionOfEventsInTails = \frac{N > EnergyThreshold}{N_{Total}} \quad (5.1)$$

where " $N > \text{Energy Threshold}$ " refers to the number of events in the tails above a given threshold and " $N_{Total}$ " refers to the total number of events.

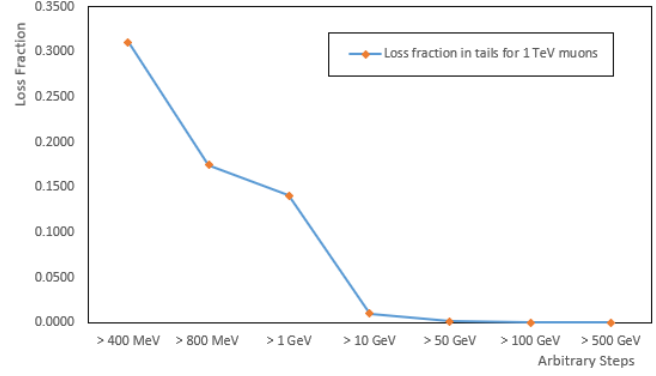
This process was used to observe the percentage of events in tails above different energy ranges/thresholds; the higher is the fraction, the higher is the probability of muons which could fake electrons/photons. This study considers muons of five different incident energies from 20 GeV, figure 5.1a, up to 1 TeV, figure 5.1b; and we have studied the percentage of events in tails above 400 MeV, 800 MeV, 1 GeV, 10 GeV, 50 GeV, 100 GeV and 500 GeV.

As expected, the fraction of muons with energy above the GeV range is very small, even for 1 TeV muons. This means that the background from these particles can be considered small.

Another representation on how muons of different energies have different percentages of events in tails is shown in figure 5.2 where all 5 simulated muons are exposed. For high energy thresholds like 500 GeV, only muons of 500 GeV and 1 TeV accomplish to record any event. 200 GeV muons just reach the 50 GeV threshold, 50 GeV muons reach the 10 GeV threshold and 20 GeV muons reach the 1 GeV threshold.



(a) 20 GeV muon.



(b) 1 TeV muon.

Figure 5.1: Fraction of events in tails for muons with 20 GeV (a) and 1 TeV (b). We observe a higher percentage of events recorded above small thresholds in high energy muons, 2.8% for (a) versus a 31% for (b). Also, for 20 GeV muons there are barely any recorded events above the 50 GeV threshold while for 1 TeV muons we still record events in tails above 500 GeV.

### 5.1.1 Parameterizations of the Energy Loss on muons

While the fraction of high momentum muons is less than 1% for thresholds above order 10 GeV, it is important to have a way to parametrise the energy loss for muons at all momentum [36]. In this section, this is done considering muons generated at different energies as described above, and observing how the energy distributions are characterised by a Landau distribution [60].

Because of the longer tails as compared to electrons we should no longer use the mean from the Gaussian fit nor the Crystal Ball. The landau function is used here to fit the long fat tails of muons which decrease algebraically. This distribution is defined by a probability density function, equation 5.2, and is shaped as shown in figure 5.3.

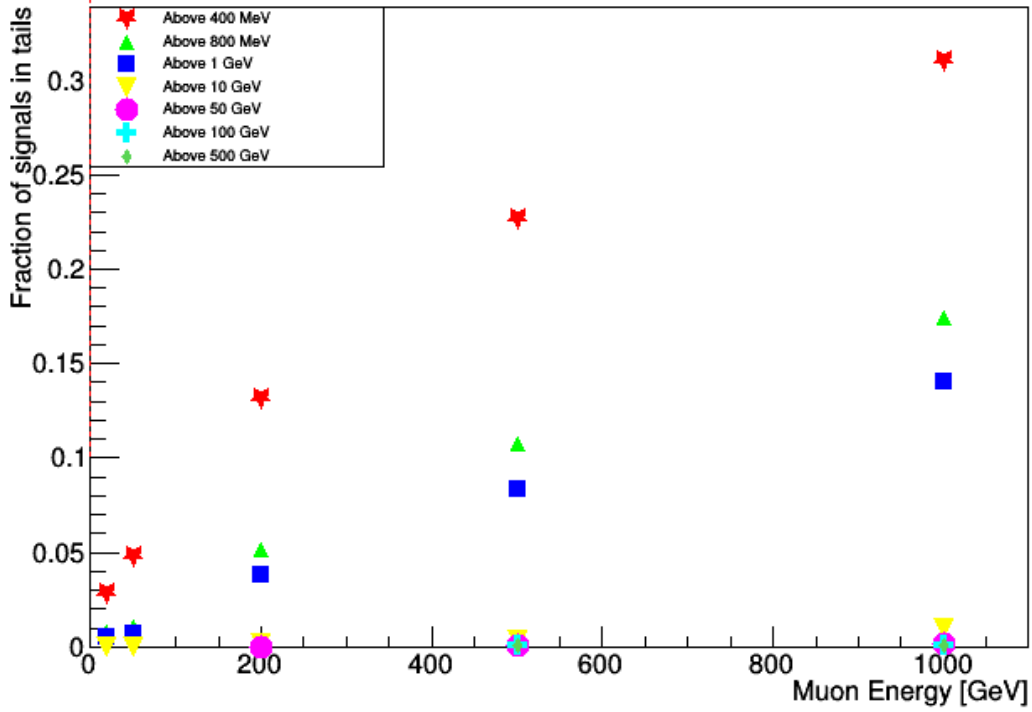


Figure 5.2: 5 simulated muons with energies increasing from 20 GeV to 1 TeV, the fraction of events in tails above the selected thresholds increase exponentially.

$$P(x; \mu, c) = \frac{1}{\pi c} \int_0^\infty e^{-t} \cos\left(t\left(\frac{x - \mu}{c}\right) + \frac{2t}{\pi} \log\left(\frac{t}{c}\right)\right) dt \quad (5.2)$$

where  $c \in (0, \infty)$  is the scale parameter and  $\mu \in (-\infty, \infty)$  is the location parameter.

As the energy increases and radiative effects become the main contributor to energy loss, we should expect this shape to start tending towards a longer tail. In this last case, although the Landau distribution is still a good parameter, it presents a bias that increases the most probable value of the fitted distribution above what the most probable energy loss should be [51].

In figure 5.4a and 5.4b, simulations for 20 GeV and 1 TeV muons showing

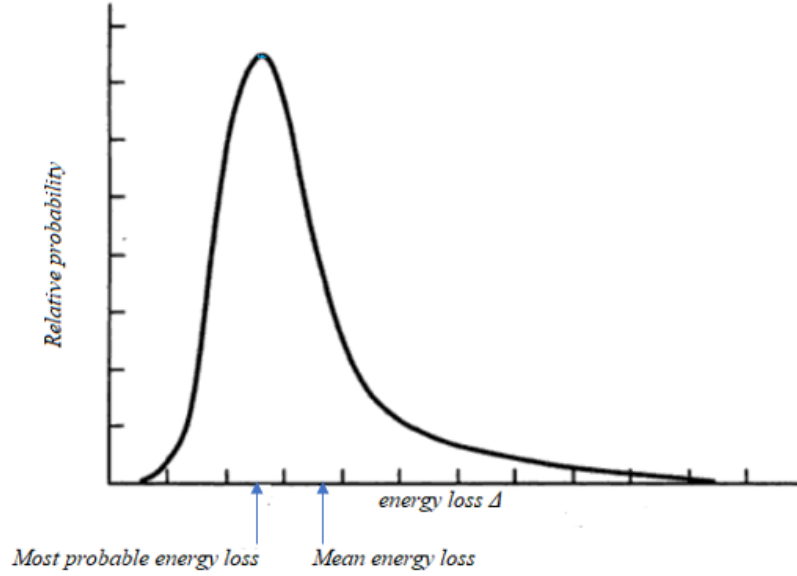


Figure 5.3: Shows the landau distribution for some relative probability. It differentiates the most probable energy loss (characteristic of this function) and the mean energy loss (given by the Gaussian fit).

a Landau fit are presented, their goal is to visualise how this described feature behaves in real sample data. Describing an accurate fit for low energy muons and slowly becoming a more asymmetrical distribution for high energetic muons.

The total loss of energy from muons traveling across the detector can be parameterized and, considering the detector is symmetric (here we are still using the original single module calorimeter configuration), this parametrization is based on the changing energies of different incident muons.

The dependence of the most probable energy loss,  $E_{loss}^{mpv}$ , as a function of the incident/injected energy,  $E_{inj}$ , is described by the following equation and presented in figure 5.5a.

$$E_{loss}^{mpv}(E_{inj}) = p_0 + p_1 \ln(E_{inj}) + p_2 E_{inj} \quad (5.3)$$

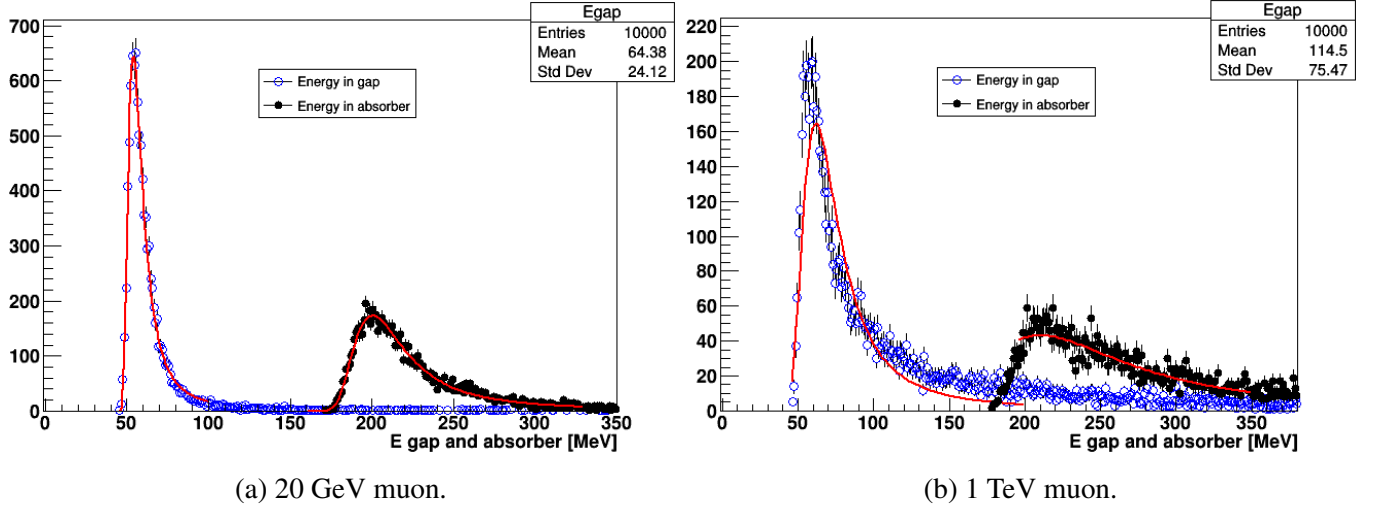


Figure 5.4: Visualization of the Landau distribution as applied on the absorber and gap energy deposits for a 20 GeV muon (a) and for a 1 TeV muon (b). It is observable how for low energies the Landau distribution presents a perfect fit but becomes more inaccurate for high energies.

where  $p_0$  describes the minimum ionizing part,  $p_1$  represents the relativistic rise, and  $p_2$  describes the radiative effects mentioned previously.

The parameterization also takes into account the width parameter,  $\sigma_{loss}$ , of the energy loss distribution. For this situation, an initial fitting method was suggested where the relativistic term was ignored, equation 5.4, [36]; although after observing this fit and realising the lack of accuracy as compared to the  $E_{loss}^{mpv}$  method, it was decided to use a fit equation with the same structure, leading us to use equation 5.5 in the study of the width, where the different elements used resemble the terms in equation 4.3.

$$\sigma_{loss}^{mpv}(E_{inj}) = p_0 + p_1 E_{inj} \quad (5.4)$$

$$\sigma_{loss}^{mpv}(E_{inj}) = p_0 + p_1 \ln(E_{inj}) + p_2 E_{inj} \quad (5.5)$$

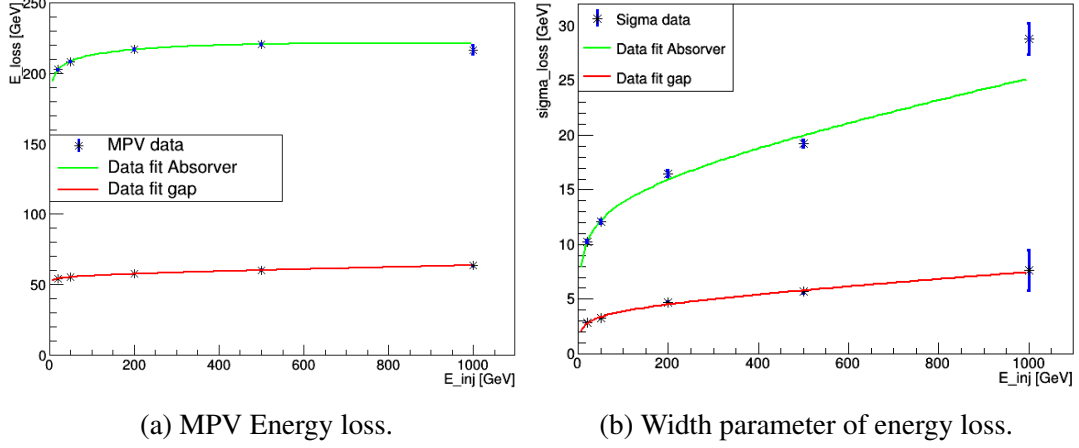


Figure 5.5: Parametrization of the MPV energy loss,  $E_{loss}^{mpv}$ , done applying equation 4.3 (a) and the width parameter of energy loss,  $\sigma_{loss}^{mpv}$ , done applying equation 4.5 (b); where the Landau distribution was considered as a function of energy. In red is the fit on the gap and in green the fit on the absorber. These consider muons of different energies accessing a single module layout calorimeter.

NAME	VALUE	ERROR	STEP SIZE	FIRST DERIVATIVE
<b>MPV Absorber Data</b>				
P0	1.8224E+02	1.2232E+00	1.8587E-04	3.1828E-08
P1	6.8059E+00	3.7467E-01	4.7194E-05	1.1425E-07
P2	-8.3650E-03	2.7966E-03	1.1518E-06	2.4464E-06
<b>MPV Gap Data</b>				
P0	5.1382E+01	2.7537E-01	7.0787E-05	9.4481E-08
P1	9.8184E-01	8.1462E-02	1.7988E-05	3.6810E-07
P2	5.6431E-03	4.8770E-04	3.6471E-07	1.2213E-05

Table 5.1: Shows the parametrization values for the MPV Energy loss absorber and gap data fit obtained for the equation presented above which can be seen to fit the landau distribution on the upper side of figure 5.5a.



NAME	VALUE	ERROR	STEP SIZE	FIRST DERIVATIVE
<b>Sigma Absorber Data</b>				
P0	4.5869E+00	6.7339E-01	1.7863E-04	-8.8006E-09
P1	1.8476E+00	2.0939E-01	4.6513E-05	-1.1085E-07
P2	2.8534E-03	1.5144E-03	1.1059E-06	-1.3015E-05
<b>Sigma Gap Data</b>				
P0	1.1322E+00	1.8203E-01	4.7616E-05	-5.6519E-08
P1	5.4174E-01	5.3594E+04	1.2193E-05	-1.4714E-07
P2	2.5949E+03	4.5497E-04	3.4022E-07	5.7956E-06

Table 5.2: Shows the parametrization values for the width loss absorber and gap data fit obtained for the equation presented above which can be seen to fit the landau distribution on the upper side of figure 5.5b.

Observing the results from this study we can conclude that the agreement between the Geant4 values and the parametrization can be evaluated as correct.

## 5.2 A word on pions

As part of this study, we have also investigated the lightest mesons,  $\pi^+$  and  $\pi^-$  [66], which deposit a much smaller amount of energy in the detector, although neutral pions,  $\pi^0$ , would deposit an increased amount of energy in comparison.

$\pi^0$  decays through the electromagnetic force as compared to charged pions which can only decay via the weak force. Because it decays via the EM force, the dominant decay mode for neutral pions is a pair of photons with a branching ratio ( $\text{BR}_{2\gamma}$ ) of 0.98823 [28].

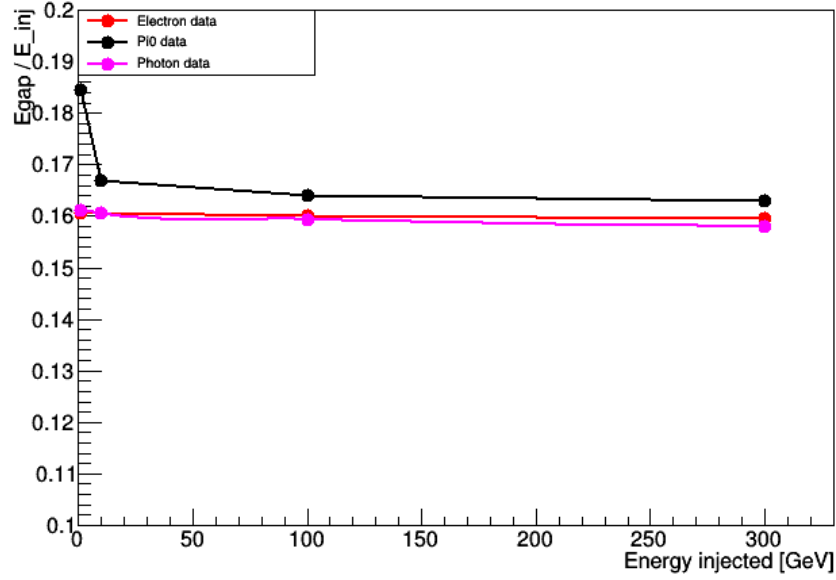
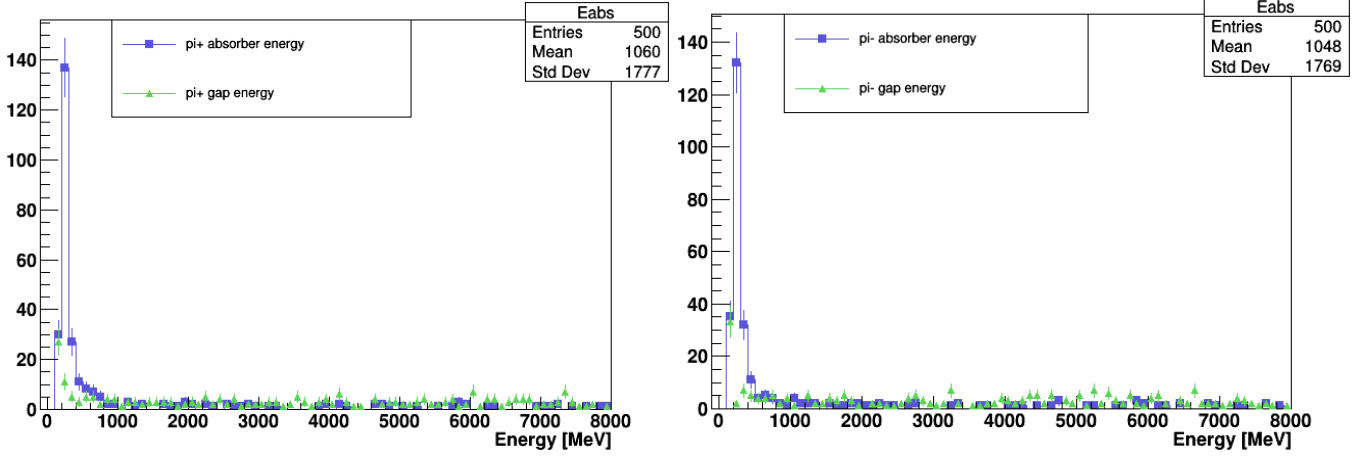


Figure 5.6: Fraction of energy deposited in the gap by the electron, photon and neutral pion using their Gaussian mean.

This type of decay makes the  $\pi^0$  deposit a fraction of energy much like that of electrons or photons as it deposits energy in the gap regions of the calorimeter, figure 5.6. This study comparing all three particle contains residual difference between  $\pi^0$  and electrons/photons because electrons and photons were simulated using the simple calorimeter layout.

We can observe how the main difference between neutral pions and electron/photon data is on the lower energy section, very low pT neutral pions (1 GeV) show a slightly higher energy fraction, one reason of this happening could be due to the differences in the showering of electrons and photons.

$\pi^+$  and  $\pi^-$  usually decay to a pair of  $\mu^+$  -  $V_\mu$  so, their signals are diluted and very little is reconstructed, to study them properly we would require an hadronic calorimeter.



(a) Deposit from  $\pi^+$ .

(b) Deposit from  $\pi^-$ .

Figure 5.7: Results from simulating a pion (a) and an anti-pion (b) at 100 GeV moving across the FASER Detector, in the X axis we find the energies and in the Y axis the number of events. Both figures show a similar behaviour where the energy deposited in the detector is around 220-250 MeV. The low and long tails extend close to 80 GeV, outside the ranges in this visualization.

On figures 5.7a and 5.7b, we observe how little energy is deposited for  $\pi^+$  and  $\pi^-$  simulated with 100 GeV. They present a negative skewed distribution, with a peak on the absorber data placed in the low energies, order of a couple hundreds of MeV, and then leading to long tails. For the gap, we seem to only record their tails starting on the low energies as well. We seem to appreciate 4 times more energy released in the absorber. These key differences sustain the claim that electrons will be detected by FASER more often than pions.

Although, the pairs  $e^+ e^-$  and  $\pi^+ \pi^-$  can be around 45% and 10% of the signal of a Dark Photon respectively, from these results we can conclude that FASER, not having an hadronic calorimeter, won't be sensitive to Dark Photons decaying into  $\pi^+ \pi^-$ .

# Chapter 6

## Summary and conclusion

In this Master's thesis we have introduced the FASER experiment and the physics background under which it operates. We have described the accelerator physics' technologies used in this innovative detector, the sector of physics it tackles to observe from the introduction of the Standard Model to the Physics Beyond Colliders program and we have provided a wide explanation on Geant4, the software chosen to investigate several calorimeter layouts and how they respond to incoming particles.

The two calorimeters studied included a simple design featuring a single module layout while the second was a more realistic design featuring four 66-layer modules separated by a gap of air of 0.2 mm in the X axis and 1.2 mm in the Y axis.

We have presented a variety of studies on the calorimeter response to particles relevant to Dark Photons at the FASER experiment. The particles studied include: electrons, photons, muons and pions (charged and neutral).

In these studies we identified how for particles interacting strongly with the

modules of the calorimeter. Electrons, photons and neutral pions deposit a fraction of energy in the gap of the calorimeter around 16% with low dependence on the injected energy of the particles up to 1 TeV.

The angular scan performed with electrons under the more realistic layout of the calorimeter, identified two case-scenarios to consider when measuring real-data from this experiment. On the one hand, we can encounter a beam moving straight through the gap between the modules of the detector without interacting, in this situation particles barely deposit any energy and leave the detector unmeasured. On the other hand, we find particles reaching the module of the detector releasing showers and depositing energy that can be measured by the gap components of the ECAL module.

We applied in the more realistic design of FASER a shift angle of 50 mrad in the X axis, as it is expected to be in the real experiment, to avoid particles moving straight from IP1 going through the gaps between the modules and not depositing any energy. What this angular scan revealed is that a particle entering the detector with a trajectory of -50 mrad in the X axis with respect to the position of FASER, will compensate this shift angle and we will expect this particle to move through the gap without interacting. Hence, creating a blind spot.

The studies performed on muons confirmed their behaviour as minimum ionising particles and we showed how the energy loss ( $E_{loss}$ ) can be parameterized well as a function of the muon initial energy.

Finally, we analysed the fraction of energy deposits expected for charged pions to confirm their low energy deposits in the EM calorimeter of FASER. Then, these charged pions cannot be detected successfully by FASER as an hadronic calorimeter would be needed for this purpose.

# Bibliography

- [1] Dark photon. [https://en.wikipedia.org/wiki/Dark\\_photon](https://en.wikipedia.org/wiki/Dark_photon).
- [2] Root software. <https://root.cern.ch/>.
- [3] High-Luminosity Large Hadron Collider (HL-LHC): Technical Design Report V. 0.1. *CERN Yellow Rep. Monogr.*, 4:1–516, 2017.
- [4] G. Aad, T. Abajyan, B. Abbott, J. Abdallah, S. Abdel Khalek, A.A. Abdellalim, O. Abdinov, R. Aben, B. Abi, M. Abolins, and et al. Observation of a new particle in the search for the standard model higgs boson with the atlas detector at the lhc. *Physics Letters B*, 716(1):1–29, Sep 2012.
- [5] Cristina Agrigoroae. Faser: Cern approves new experiment to look for long-lived, exotic particles. <https://home.cern/news/news/experiments/faser-cern-approves-new-experiment-look-long-lived-exotic-particles> 03 2019.
- [6] Jamie Boyd David W. Casper 4 Jonathan L. Feng Iftah Galon 5 Shih-Chieh Hsu 6 Felix Kling-Hidetoshi Otono-2 Brian Petersen Osamu Sato Aaron M.

- Soffa Jeffrey R. Swaney Akitaka Ariga, 1 Tomoko Ariga and Sebastian Trojanowski. Letter of intent: Faser forward search experiment at the lh. pages 16–17, 07 2018.
- [7] Jamie Boyd Franck Cadoux David W. Casper Yannick Favre Jonathan L. Feng 5 Didier Ferrere Iftah Galon Sergio Gonzalez-Sevilla Shih-Chieh Hsu Giuseppe Iacobucci Enrique Kajomovitz Felix Kling Susanne Kuehn Lorne Levinson Hidetoshi Otono 2 Brian Petersen Osamu Sato Matthias Schott Anna Sfyrta Jordan Smolinsky Aaron M. Soffa Yosuke Takubo Eric Torrence Sebastian Trojanowski Akitaka Ariga, Tomoko Ariga and Gang Zhang. Faser’s physics reach for long-lived particles. page 7, 2019.
- [8] Jamie Boyd Franck Cadoux David W. Casper Yannick Favre Jonathan L. Feng † Didier Ferrere Iftah Galon Sergio Gonzalez-Sevilla-Gang Zhang Akitaka Ariga, Tomoko Ariga et al. Faser: Forward search experiment at the lh. page 8, December 2018.
- [9] Carl D. Anderson. The apparent existence of easily deflectable positives. *Science*, 76(1967), 9 1932.
- [10] Akitaka Ariga, Tomoko Ariga, Jamie Boyd, Franck Cadoux, David W. Casper, Yannick Favre, Jonathan L. Feng, Didier Ferrere, Iftah Galon, Sergio Gonzalez-Sevilla, and et al. Faser’s physics reach for long-lived particles. *Physical Review D*, 99(9), May 2019.
- [11] arXiv:1901.04468UCI-TR2019-01KYUSHU-RCAPP-2018-08 Ariga, Akitaka et al. FASER: ForwArd Search ExpeRiment at the LHC.

- [12] Makoto ASAI. Introduction to geant4. <https://geant4.web.cern.ch/sites/geant4.web.cern.ch/files/geant4/support/training/CSC2000/CSCG4.pdf>.
- [13] Brian Batell, Ayres Freitas, Ahmed Ismail, and David McKeen. Flavor-specific scalar mediators. *Physical Review D*, 98(5), Sep 2018.
- [14] Marco Battaglieri, Alberto Belloni, Aaron Chou, Priscilla Cushman, and et al. Us cosmic visions: New ideas in dark matter 2017: Community report, 2017.
- [15] Martin Bauer, Patrick Foldenauer, and Joerg Jaeckel. Hunting all the hidden photons. *Journal of High Energy Physics*, 2018(7), Jul 2018.
- [16] J Beacham, C Burrage, D Curtin, A De Roeck, J Evans, J L Feng, C Gatto, S Gninenko, A Hartin, I Irastorza, and et al. Physics beyond colliders at cern: beyond the standard model working group report. *Journal of Physics G: Nuclear and Particle Physics*, 47(1):010501, Dec 2019.
- [17] H.A. Bethe and W. Heitler. 1934.
- [18] Diego Bettoni. The standard model lagrangian. <http://www.fe.infn.it/~bettoni/particelle/Strong/SMLagrangian.pdf>.
- [19] J. B. Birks. Scintillations from organic crystals: Specific fluorescence and relative response to different radiations. *Proceedings of the Physical Society*, 64(10), 1951.
- [20] Jamie Boyd. FASER - CERN Detector Seminar 17/4/2020. <https://indico.cern.ch/>.



- [21] et al C. Allanach. Beyond the standard model physics at the hl-lhc and he-lhc. page 9, 8 2019.
- [22] et al C. Allanach. Beyond the standard model physics at the hl-lhc and he-lhc. page 91, 8 2019.
- [23] J. Chadwick. Possible existence of a neutron. *Nature*, 129(3252), 2 1932.
- [24] S. Chatrchyan, V. Khachatryan, A.M. Sirunyan, A. Tumasyan, W. Adam, E. Aguilo, T. Bergauer, M. Dragicevic, J. Erö, C. Fabjan, and et al. Observation of a new boson at a mass of 125 gev with the cms experiment at the lhc. *Physics Letters B*, 716(1):30–61, Sep 2012.
- [25] ATLAS collaboration. TAS-TAN. <https://espace.cern.ch/efthymio/Wiki%20Pages/TAS-TAN.aspx>.
- [26] FASER Collaboration, Akitaka Ariga, Tomoko Ariga, Jamie Boyd, David W. Casper, Jonathan L. Feng, Iftah Galon, Shih-Chieh Hsu, Felix Kling, Hidetoshi Otono, Brian Petersen, Osamu Sato, Aaron M. Soffa, Jeffrey R. Swaney, and Sebastian Trojanowski. Letter of intent for faser: Forward search experiment at the lhc, 2018.
- [27] Many contributors. Calorimeter (Particle Physics) .
- [28] Many contributors. Pion - wikipedia. [https://en.wikipedia.org/wiki/Pion#Neutral\\_pion\\_decays](https://en.wikipedia.org/wiki/Pion#Neutral_pion_decays), 2020.
- [29] W. N. Cottingham and D. A. Greenwood. Standard Model Lagrangian from An Introduction to the Standard Model of Particle Physics . [http://einstein-schrodinger.com/Standard\\_Model.pdf](http://einstein-schrodinger.com/Standard_Model.pdf).

- [30] K.A. Olive et al. Pparticle detectors. *Particle Data Group*, (2014) and 2015 update(38), 2015.
- [31] S.Agostinelli et al. Geant4 - ExampleB4. [http://geant4-userdoc.web.cern.ch/geant4-userdoc/Doxygen/examples\\_doc/html/ExampleB4.html](http://geant4-userdoc.web.cern.ch/geant4-userdoc/Doxygen/examples_doc/html/ExampleB4.html).
- [32] S.Agostinelli et al. Geant4 software. <https://geant4.web.cern.ch/>.
- [33] Lyndon Evans. The large hadron collider. *New Journal of Physics*, 9(9):335–335, sep 2007.
- [34] P. Collier-E. Elsen (via video) D. Forkel-Wirth F. Forti R. Forty (Secretary) F. Gianotti (Chair) G. Giudice F. Hemmer-J.M. Jimenez K. Johnston M. Kramer R. Losito L. Miralles J. Nash (via video) B. Petersen K. Riisager (via video) H. Wilkens F. Bordry, T. Cass. Letter of intent: Minutes of the 228th meeting of the research board held on friday 5 march 2019. 03 2019.
- [35] Christian W. Fabjan and Fabiola Gianotti. Calorimetry for particle physic. page 6, 10 2003.
- [36] Christian W. Fabjan and Fabiola Gianotti. Muons in the calorimeters: Energy loss corrections and muon tagging. pages 5–6, 4 2009.
- [37] Deion Fellers. Faser fast calorimeter simulation, 3 2020.
- [38] James Feng, Jonathan; Boyd. Technical proposal: Faser, the forward search experiment at the lhc. 12 2018.

- [39] Jonathan L. Feng, Iftah Galon, Felix Kling, and Sebastian Trojanowski. Axionlike particles at faser: The lhc as a photon beam dump. *Physical Review D*, 98(5), Sep 2018.
- [40] Jonathan L. Feng, Iftah Galon, Felix Kling, and Sebastian Trojanowski. Dark higgs bosons at the forward search experiment. *Physical Review D*, 97(5), Mar 2018.
- [41] Jonathan L. Feng, Iftah Galon, Felix Kling, and Sebastian Trojanowski. Forward search experiment at the lhc. *Physical Review D*, 97(3), Feb 2018.
- [42] William Frass. C4: Particle physics major option, particle detectors. <https://www2.physics.ox.ac.uk/sites/default/files/Detectors.pdf>.
- [43] Oscar Miyamoto Gomez. Five mysteries the standard model can't explain. <https://www.symmetrismagazine.org/article/five-mysteries-the-standard-model-cant-explain>.
- [44] Juan Carlos Helo, Martin Hirsch, and Zeren Simon Wang. Heavy neutral fermions at the high-luminosity lhc. *Journal of High Energy Physics*, 2018(7), Jul 2018.
- [45] Eder Izaguirre, Gordan Krnjaic, Philip Schuster, and Natalia Toro. Analyzing the discovery potential for light dark matter. *Physical Review Letters*, 115(25), Dec 2015.
- [46] J. D. Jackson. Kinematics. <http://pdg.lbl.gov/2005/reviews/kinemarpp.pdf>, 2004.

- [47] Felix Kling Jonathan L. Feng, Iftah Galon and Sebastian Trojanowski. Faser: Forward search experiment at the lhc. 08 2017.
- [48] Gerfried J Wiener Julia Woithe and Frederik F Van der Veken1. Let's have a coffee with the standard model of particle physics! <https://iopscience.iop.org/article/10.1088/1361-6552/aa5b25/pdf>.
- [49] S.R. Keiner and Yu. D. Kotov. 1968.
- [50] Felix Kling and Sebastian Trojanowski. Heavy neutral leptons at faser. *Physical Review D*, 97(9), May 2018.
- [51] E W ; Salzburger A Lopez Mateos, D ; Hughes. A parameterization of the energy loss of muons in the atlas tracking geometry. (ATL-MUON-PUB-2008-002), 1 2008.
- [52] many other contributors. Calculation of radiation length in materials. <https://cds.cern.ch/record/1279627/files/PH-EP-Tech-Note-2010-013.pdf>.
- [53] many other contributors. Calorimeters - energy measurement. [https://www.desy.de/~garutti/LECTURES/ParticleDetectorSS12/L10\\_Calorimetry.pdf](https://www.desy.de/~garutti/LECTURES/ParticleDetectorSS12/L10_Calorimetry.pdf).
- [54] many other contributors. FASER - CALORIMETER. <https://faser.web.cern.ch/about-the-experiment/detector-design/calorimeter>.

- [55] many other contributors. FASER - Location of the Experiment. <https://faser.web.cern.ch/about-the-experiment/location>.
- [56] many other contributors. FASER in a Nutshell - Discovery Prospects for FASER. [https://twiki.cern.ch/twiki/bin/view/FASER/WebHome#FASER\\_in\\_a\\_Nutshell](https://twiki.cern.ch/twiki/bin/view/FASER/WebHome#FASER_in_a_Nutshell).
- [57] many other contributors. FASER in a Nutshell - Welcome to the FASER Webpage. [https://twiki.cern.ch/twiki/bin/view/FASER/WebHome#FASER\\_in\\_a\\_Nutshell](https://twiki.cern.ch/twiki/bin/view/FASER/WebHome#FASER_in_a_Nutshell).
- [58] many other contributors. How a detector works. <https://home.cern/science/experiments/how-detector-works>.
- [59] many other contributors. The standard model. <https://home.cern/science/physics/standard-model>.
- [60] M. MARUCHO, C. A. GARCIA CANAL, and HUNER FANCHIOTTI. The landau distribution for charged particles traversing thin films. *International Journal of Modern Physics C*, 17(10):1461–1476, Oct 2006.
- [61] ICRR Masahiro Ibe(Tokyo U. and Shin Kobayashi(Tokyo U. ICRR) Yuhei Nakayama(Tokyo U. ICRR) Satoshi Shirai(Tokyo U. IPMU) Tokyo U., IPMU). Cosmological constraint on dark photon from  $n_e f f$ . 122019.
- [62] Stefano Meroli. Multiple scattering for particles in matter. [https://meroli.web.cern.ch/lecture\\_multiple\\_scattering.html](https://meroli.web.cern.ch/lecture_multiple_scattering.html).

- [63] W. F.; Hurlbut C. R.; Kusner M. R. Moser, S. W.; Harder. Principles and practice of plastic scintillator design. *Radiation Physics and Chemistry*, 41(1-2):31–36, 1 1993.
- [64] Carl D. Neddermeyer, Seth H.; Anderson. Note on the nature of cosmic-ray particles. *Physical Review*, 51(10), 5 1937.
- [65] Annika H. G. Peter, Vera Gluscevic, Anne M. Green, Bradley J. Kavanagh, and Samuel K. Lee. Wimp physics with ensembles of direct-detection experiments, 2013.
- [66] D.-O. Riska. Few-body problems in physics '02: Pion decay of heavy-light mesons. page 19, 2003.
- [67] Rogerio Rosenfeld. Introduction to the standard model. [http://www.ifsc.usp.br/~lattice/Natal\\_1.pdf](http://www.ifsc.usp.br/~lattice/Natal_1.pdf).
- [68] B. Rossi. High energy particles. page 16, 1952.
- [69] J. M. Katzy E. Yatsenko T. Pierog, I. Karpenko and K. Werner. Epos lhc: Test of collective hadronization with data measured at the cern large hadron collider. 12 2015.
- [70] Sebastian Trojanowski. Looking forward to new physics with faser: Forward search experiment at the lhc. <https://www2.physics.ox.ac.uk/sites/default/files/page/2012/03/27/trojanowski-faser-oxford-jan2019-44495.pdf>, 1 2019.
- [71] F. G.; Murphy G. M Urey, Harold C.; Brickwedde. A hydrogen isotope of mass 2. *Physical Review D*, 39(1), 1931.

- [72] X. Cid Vidal, M. D’Onofrio, P. J. Fox, R. Torre, K. A. Ulmer, A. Aboubrahim, A. Albert, J. Alimena, B. C. Allanach, C. Alpigiani, and et al. Beyond the standard model physics at the hl-lhc and he-lhc, 2018.
- [73] C. Ludeling W. Buchmuller. Field theory and standard model. <https://arxiv.org/pdf/hep-ph/0609174.pdf>, 2005.

## Appendix

Benchmark Model	Label	PBC	Refs	FASER	FASER 2
Dark Photons	V1	BC1	[41]	✓	✓
B - L Gauge Bosons	V2	-	[15]	✓	✓
Dark Higgs Bosons	S1	BC4	[40, 13]	-	✓
Dark Higgs Bosons with hSS	S2	BC5	[40]	-	✓
HNLs with $e$	F1	BC6	[50, 44]	-	✓
HNLs with $\mu$	F2	BC7	[50, 44]	-	✓
HNLs with $\tau$	F3	BC8	[50, 44]	✓	✓
ALPs with Photon	A1	BC9	[39]	✓	✓
ALPs with Fermion	A2	BC10	-	-	✓
ALPs with Gluon	A3	BC11	-	✓	✓
Dark Pseudoscalars	P1	-	[26]	-	✓

Table 6.1: This table, extracted from FASER’s research on the physics reach of the detector for Long-Lived Particles [10], shows a variety of benchmark models aimed to be studied by the FASER collaboration during FASER or FASER 2. The table presents the labels of each benchmark as well as their PBC labels and references where they have been previously studied. The discovery potential of FASER and FASER 2 covers candidates with renormalizable couplings like dark photons, dark Higgs bosons or HNLs (Heavy Neutral Leptons); also potential to discover ALPs (axion-like particles) with their corresponding couplings; dark pseudoscalars with Yukawa-like couplings; and others.



## CODE

### Code used to generate fraction of energy deposits studies

Macro used to generate figure 5.6.

```
{  
  
    TFile *_file1 = TFile::Open("ele_1GeV.root");  
  
    cout << " ----- 1 GeV electron -----" << endl;  
    float inj = 1000.;  
    cout << " top=abs+gap " << Eabs->GetMean()+  
    Egap->GetMean() << " (inj-tot)/inj " << (inj-(Eabs->GetMean()+Egap  
->GetMean()))/inj << endl;  
    cout << " abs " << Eabs->GetMean() << "+/-" << Eabs->GetRMS() << endl;  
    cout << " gap " << Egap->GetMean() << "+/-" << Egap->GetRMS() << endl;  
  
    cout << " ----- " << endl;  
  
    float res_1GeV = (inj-(Eabs->GetMean()+Egap->GetMean()))/inj;  
    float res_1GeV = Egap->GetMean()/inj;  
  
    TFile *_file2 = TFile::Open("ele_10GeV.root");  
    inj = 10000.;  
    cout << " ----- 10 GeV electron -----" << endl;
```

```

cout << " top=abs+gap " << Eabs->GetMean()+Egap->GetMean() <<
" (inj-tot)/inj " << (inj-(Eabs->GetMean()+Egap->GetMean()))/inj << endl;
cout << " abs " << Eabs->GetMean() << "+/-" << Eabs->GetRMS() << endl;
cout << " gap " << Egap->GetMean() << "+/-" << Egap->GetRMS() << endl;
cout << " ----- "
<< endl;
// float res_10GeV = (inj-(Eabs->GetMean()+Egap->GetMean()))/inj;
float res_10GeV = Egap->GetMean()/inj;

```

```

TFile *_file3 = TFile::Open("ele_100GeV.root");
inj = 100000.;
cout << " ----- 100 GeV electron -----" << endl;
cout << " top=abs+gap " << Eabs->GetMean()+Egap->GetMean() <<
"(inj-tot)/inj " << (inj-(Eabs->GetMean()+Egap->GetMean()))/inj << endl;
cout << " abs " << Eabs->GetMean() << "+/-" << Eabs->GetRMS() << endl;
cout << " gap " << Egap->GetMean() << "+/-" << Egap->GetRMS() << endl;
cout << " -----
// float res_100GeV = (inj-(Eabs->GetMean()+Egap->GetMean()))/inj;
float res_100GeV = Egap->GetMean()/inj;

```

```

\tt TFile *_file4 = TFile::Open("ele_300GeV.root");
inj = 300000.;
cout << " ----- 300 GeV electron -----" << endl;
cout << " top=abs+gap " << Eabs->GetMean()+Egap->GetMean() <<
" (inj-tot)/inj " << (inj-(Eabs->GetMean()+Egap->GetMean()))/inj << endl;

```

```

cout << " abs " << Eabs->GetMean() << "+/-" << Eabs->GetRMS() << endl;
cout << " gap " << Egap->GetMean() << "+/-" << Egap->GetRMS() << endl;
cout << " -----
" << endl;
// float res_500GeV = (inj-(Eabs->GetMean()+Egap->GetMean()))/inj;
float res_300GeV = Egap->GetMean()/inj;

Double_t Graph0_fx3001[4] = {1., 10., 100., 300.};
Double_t Graph0_fy3001[4] = {res_1GeV, res_10GeV, res_100GeV, res_300GeV};
Double_t Graph0_felx3001[4] = { 0, 0, 0, 0};
Double_t Graph0_fely3001[4] = { 0, 0, 0, 0};
Double_t Graph0_fehx3001[4] = { 0, 0, 0, 0};
Double_t Graph0_fehy3001[4] = { 0, 0, 0, 0};

TGraphAsymmErrors *grae = new TGraphAsymmErrors(4,Graph0_fx3001,
Graph0_fy3001,Graph0_felx3001,Graph0_fehx3001,Graph0_fely3001,
Graph0_fehy3001);
grae->SetName("Graph0");
grae->SetTitle("Graph");
Int_t ci; // for color index setting
TColor *color; // for color definition with alpha
ci = 2;
grae->SetLineWidth(2);
grae->SetLineColor(2);
grae->SetMarkerColor(ci);

```

```

grae->SetMarkerStyle(20);
grae->SetMarkerSize(1.2);
// grae->SetTitle("Injected Energy - (Abs+Gap) Over Injected Energy");
// grae->GetXaxis()->SetTitle("Energy injected [GeV]");
// grae->GetYaxis()->SetTitle("(E_inj - E(gap+abs))/E_inj");

grae->SetTitle("Energy Gap Fraction");
grae->GetXaxis()->SetTitle("Energy injected [GeV]");
grae->GetYaxis()->SetTitle("Egap / E_inj");

grae->SetMaximum(0.2);
grae->SetMinimum(0.1);
grae->Draw("apl");

TFile *_file11 = TFile::Open("pi0_1GeV.root");

cout << " ----- 1 GeV pi 0 -----" << endl;
inj = 1000.;
cout << " top=abs+gap " << Eabs->GetMean()+Egap->GetMean() <<
" (inj-tot)/inj " << (inj-(Eabs->GetMean()+Egap->GetMean()))/inj << endl;
cout << " abs " << Eabs->GetMean() << "+/-" << Eabs->GetRMS() << endl;
cout << " gap " << Egap->GetMean() << "+/-" << Egap->GetRMS() << endl;

```

```

cout << " ----- " << endl;
// float pi0res_1GeV = (inj-(Eabs->GetMean()+Egap->GetMean()))/inj;
float pi0res_1GeV = Egap->GetMean()/inj;

TFile *_file12 = TFile::Open("pi0_10GeV.root");
inj = 10000.;
cout << " ----- 10 GeV pi 0 -----" << endl;
cout << " top=abs+gap " << Eabs->GetMean()+Egap->GetMean() <<
" (inj-tot)/inj " << (inj-(Eabs->GetMean()+Egap->GetMean()))/inj << endl;
cout << " abs " << Eabs->GetMean() << "+/-" << Eabs->GetRMS() << endl;
cout << " gap " << Egap->GetMean() << "+/-" << Egap->GetRMS() << endl;
cout << " -----
" << endl;
// float pi0res_10GeV = (inj-(Eabs->GetMean()+Egap->GetMean()))/inj;
float pi0res_10GeV = Egap->GetMean()/inj;

TFile *_file13 = TFile::Open("pi0_100GeV.root");
inj = 100000.;
cout << " ----- 100 GeV pi0 -----" << endl;
cout << " top=abs+gap " << Eabs->GetMean()+Egap->GetMean() <<
" (inj-tot)/inj " << (inj-(Eabs->GetMean()+Egap->GetMean()))/inj << endl;
cout << " abs " << Eabs->GetMean() << "+/-" << Eabs->GetRMS() << endl;
cout << " gap " << Egap->GetMean() << "+/-" << Egap->GetRMS() << endl;
cout << " -----
" << endl;

```

```

// float pi0res_100GeV = (inj-(Eabs->GetMean()+Egap->GetMean()))/inj;
float pi0res_100GeV = Egap->GetMean()/inj;

TFile *_file14 = TFile::Open("pi0_300GeV.root");
inj = 300000.;
cout << " ----- 300 GeV pi0 -----" << endl;
cout << " top=abs+gap " << Eabs->GetMean()+Egap->GetMean() <<
" (inj-tot)/inj " << (inj-(Eabs->GetMean()+Egap->GetMean()))/inj << endl;
cout << " abs " << Eabs->GetMean() << "+/-" << Eabs->GetRMS() << endl;
cout << " gap " << Egap->GetMean() << "+/-" << Egap->GetRMS() << endl;
cout << " -----
" << endl;
// float pi0res_300GeV = (inj-(Eabs->GetMean()+Egap->GetMean()))/inj;
float pi0res_300GeV = Egap->GetMean()/inj;

Double_t Graph1_fx3001[4] = {1., 10., 100., 300.};
Double_t Graph1_fy3001[4] = {pi0res_1GeV, pi0res_10GeV, pi0res_100GeV, pi0re
Double_t Graph1_felx3001[4] = { 0, 0, 0, 0};
Double_t Graph1_fely3001[4] = { 0, 0, 0, 0};
Double_t Graph1_fehx3001[4] = { 0, 0, 0, 0};
Double_t Graph1_fehy3001[4] = { 0, 0, 0, 0};

TGraphAsymmErrors *grae2 = new TGraphAsymmErrors(4,Graph1_fx3001,

```

```

Graph1_fy3001,Graph1_felx3001,Graph1_fehx3001,Graph1_fely3001,
Graph1_fehy3001);
grae2->SetName("Graph02");
grae2->SetTitle("Graph2");
grae2->SetLineWidth(2);
grae2->SetLineColor(1);
grae2->SetMarkerColor(1);
grae2->SetMarkerStyle(20);
grae2->SetMarkerSize(1.2);
grae2->Draw("pl");

```

```

TFile *_file21 = TFile::Open("gamma_1GeV.root");

```

```

cout << " ----- 1 GeV photon -----" << endl;
inj = 1000.;
cout << " top=abs+gap " << Eabs->GetMean()+Egap->GetMean() << " (inj-tot)/in
cout << " abs " << Eabs->GetMean() << "+/-" << Eabs->GetRMS() << endl;
cout << " gap " << Egap->GetMean() << "+/-" << Egap->GetRMS() << endl;
cout << " -----
" << endl;
// float pi0res_1GeV = (inj-(Eabs->GetMean()+Egap->GetMean()))/inj;
float gammares_1GeV = Egap->GetMean()/inj;

```

```

TFile *_file22 = TFile::Open("gamma_10GeV.root");
inj = 10000.;
cout << " ----- 10 GeV photon -----" << endl;
cout << " top=abs+gap " << Eabs->GetMean()+Egap->GetMean() <<
" (inj-tot)/inj " << (inj-(Eabs->GetMean()+Egap->GetMean()))/inj << endl;
cout << " abs " << Eabs->GetMean() << "+/-" << Eabs->GetRMS() << endl;
cout << " gap " << Egap->GetMean() << "+/-" << Egap->GetRMS() << endl;
cout << " -----
" << endl;
// float pi0res_10GeV = (inj-(Eabs->GetMean()+Egap->GetMean()))/inj;
float gammares_10GeV = Egap->GetMean()/inj;

TFile *_file23 = TFile::Open("gamma_100GeV.root");
inj = 100000.;
cout << " ----- 100 GeV photon -----" << endl;
cout << " top=abs+gap " << Eabs->GetMean()+Egap->GetMean() <<
" (inj-tot)/inj " << (inj-(Eabs->GetMean()+Egap->GetMean()))/inj << endl;
cout << " abs " << Eabs->GetMean() << "+/-" << Eabs->GetRMS() << endl;
cout << " gap " << Egap->GetMean() << "+/-" << Egap->GetRMS() << endl;
cout << " -----
" << endl;
// float pi0res_100GeV = (inj-(Eabs->GetMean()+Egap->GetMean()))/inj;
float gammares_100GeV = Egap->GetMean()/inj;

```



```

TFile *_file24 = TFile::Open("gamma_300GeV.root");
inj = 300000.;
cout << " ----- 300 GeV photon -----" << endl;
cout << " top=abs+gap " << Eabs->GetMean()+Egap->GetMean() <<
" (inj-tot)/inj " << (inj-(Eabs->GetMean()+Egap->GetMean()))/inj << endl;
cout << " abs " << Eabs->GetMean() << "+/-" << Eabs->GetRMS() << endl;
cout << " gap " << Egap->GetMean() << "+/-" << Egap->GetRMS() << endl;
cout << " -----
" << endl;
// float pi0res_300GeV = (inj-(Eabs->GetMean()+Egap->GetMean()))/inj;
float gammares_300GeV = Egap->GetMean()/inj;

Double_t Graph2_fx3001[4] = {1., 10., 100., 300.};
Double_t Graph2_fy3001[4] = {gammares_1GeV, gammares_10GeV, gammares_100GeV,
Double_t Graph2_felx3001[4] = { 0, 0, 0, 0};
Double_t Graph2_fely3001[4] = { 0, 0, 0, 0};
Double_t Graph2_fehx3001[4] = { 0, 0, 0, 0};
Double_t Graph2_fehy3001[4] = { 0, 0, 0, 0};

TGraphAsymmErrors *grae3 = new TGraphAsymmErrors(4,Graph2_fx3001,
Graph2_fy3001,Graph2_felx3001,Graph2_fehx3001,Graph2_fely3001,
Graph2_fehy3001);
grae3->SetName("Graph03");
grae3->SetTitle("Graph3");

```

```

grae3->SetLineWidth(2);
grae3->SetLineColor(6);
grae3->SetMarkerColor(6);
grae3->SetMarkerStyle(20);
grae3->SetMarkerSize(1.2);
grae3->Draw("cp");

    auto legend = new TLegend(0.1, 0.8, 0.35, 0.9);
legend->AddEntry(grae, "Electron data", "apl");
legend->AddEntry(grae2, "Pi0 data", "apl");
legend->AddEntry(grae3, "Photon data", "apl");
legend->Draw();

}

```

### Code used to generate particles through Geant 4

Code used to generate particles and to assign the characteristics to simulate including the shift angle, the entrance coordinates, the angle of the trajectory...

```

///
// *****
// * License and Disclaimer *
// *
// * The Geant4 software is copyright of the Copyright Holders of *
// * the Geant4 Collaboration. It is provided under the terms and *
// * conditions of the Geant4 Software License, included in the file *
// * LICENSE and available at http://cern.ch/geant4/license . These *
// * include a list of copyright holders. *
// *
// * Neither the authors of this software system, nor their employing *
// * institutes, nor the agencies providing financial support for this *
// * work make any representation or warranty, express or implied, *
// * regarding this software system or assume any liability for its *
// * use. Please see the license in the file LICENSE and URL above *
// * for the full disclaimer and the limitation of liability. *
// *
// * This code implementation is the result of the scientific and *
// * technical work of the GEANT4 collaboration. *
// * By using, copying, modifying or distributing the software (or

```

```

// * any work based on the software) you agree to acknowledge its *
// * use in resulting scientific publications, and indicate your *
// * acceptance of all terms of the Geant4 Software license.      *
// *****
// $Id: B4PrimaryGeneratorAction.cc 100946 2016-11-03 11:28:08Z gcosmo $
//
/// \file B4PrimaryGeneratorAction.cc
/// \brief Implementation of the B4PrimaryGeneratorAction class

#include "B4PrimaryGeneratorAction.hh"
#include "G4RunManager.hh"
#include "G4LogicalVolumeStore.hh"
#include "G4LogicalVolume.hh"
#include "G4Box.hh"
#include "G4Event.hh"
#include "G4ParticleGun.hh"
#include "G4ParticleTable.hh"
#include "G4ParticleDefinition.hh"
#include "G4SystemOfUnits.hh"
#include "Randomize.hh"

//....oooO0000ooo.....oooO0000ooo.....oooO0000ooo.....

B4PrimaryGeneratorAction::B4PrimaryGeneratorAction()
: G4VUserPrimaryGeneratorAction(),

```

```

    fParticleGun(nullptr)
{
    G4int nofParticles = 1;
    fParticleGun = new G4ParticleGun(nofParticles);

    // default particle kinematic
    //
    auto particleDefinition
        = G4ParticleTable::GetParticleTable()->FindParticle("e-");
    fParticleGun->SetParticleDefinition(particleDefinition);
    // fParticleGun->SetParticleMomentumDirection(G4ThreeVector(0.,0.,1.));
    double angle = 0. *deg;
    // double angle = 0.572958 *deg; // 10 mradian
    // double angle = 1.145916 *deg; // 20 mradian
    // double angle = 1.718874 *deg; // 30 mradian
    // double angle = 2.86479 *deg; // 50 mradian
    // double angle = 4.583664 *deg; // 80 mradian
    // double angle = 5.72958 *deg; // 100 mradian
    // double angle = -0.572958 *deg; // -10 mradian
    // double angle = -1.145916 *deg; // -20 mradian
    // double angle = -1.718874 *deg; // -30 mradian
    // double angle = -2.86479 *deg; // -50 mradian
    // double angle = -4.583664 *deg; // -80 mradian
    // double angle = -5.72958 *deg; // -100 mradian

```

```

// new default beam must be 50 mrad displaced along x-axis
double shiftangle = 2.86479 *deg;
fParticleGun->SetParticleMomentumDirection(G4ThreeVector
(std::sin(angle+shiftangle),0.,std::cos(angle)));
fParticleGun->SetParticleEnergy(50.*MeV);
}
//.....ooo00000ooo.....ooo00000ooo.....ooo00000ooo.....
B4PrimaryGeneratorAction::~B4PrimaryGeneratorAction()
{
    delete fParticleGun;
}
//.....ooo00000ooo.....ooo00000ooo.....ooo00000ooo.....

void B4PrimaryGeneratorAction::GeneratePrimaries(G4Event* anEvent)
{
    // This function is called at the begining of event

    // In order to avoid dependence of PrimaryGeneratorAction
    // on DetectorConstruction class we get world volume
    // from G4LogicalVolumeStore
    //
    G4double worldZHalfLength = 0.;
    auto worldLV = G4LogicalVolumeStore::GetInstance()->GetVolume("World");

    // Check that the world volume has box shape

```

```

G4Box* worldBox = nullptr;
if ( worldLV ) {
    worldBox = dynamic_cast<G4Box*>(worldLV->GetSolid());
}
if ( worldBox ) {
    worldZHalfLength = worldBox->GetZHalfLength();
}
else {
    G4ExceptionDescription msg;
    msg << "World volume of box shape not found." << G4endl;
    msg << "Perhaps you have changed geometry." << G4endl;
    msg << "The gun will be place in the center.";
    G4Exception("B4PrimaryGeneratorAction::GeneratePrimaries()",
        "MyCode0002", JustWarning, msg);
}
// Set gun position
// fParticleGun
//   ->SetParticlePosition(G4ThreeVector(0., 0.,
// -worldZHalfLength));
// move position if center is inactive
fParticleGun
    ->SetParticlePosition(G4ThreeVector(10.*mm, -10.*mm,
    -worldZHalfLength));
fParticleGun->GeneratePrimaryVertex(anEvent);
}

```

